Dense connectomic reconstruction in layer 4 of the somatosensory cortex
— **Source link** ↗

Alessandro Motta, Manuel Berning, Kevin M Boergens, Benedikt Staffler ...+6 more authors

Institutions: Max Planck Society

Topics: Barrel cortex, Neuropil and Cortex (anatomy)

Related papers:

- Nanoconnectomic upper bound on the variability of synaptic plasticity

- Distribution and strength of interlaminar synaptic connectivity in mouse primary visual cortex revealed by two-photon optogenetic stimulation

- Axonal synapse sorting in medial entorhinal cortex

- The Excitatory Neuronal Network of the C2 Barrel Column in Mouse Primary Somatosensory Cortex

- Cell type specificity of local cortical connections.

Dense connectomic reconstruction in layer 4 of the somatosensory cortex

Alessandro Motta[1]*, Manuel Berning[1]*, Kevin M. Boergens[1]*, Benedikt Staffler[1]*, Marcel Beining[1], Sahil Loomba[1], Christian Schramm[1], Philipp Hennig[2], Heiko Wissler[1], Moritz Helmstaedter[1]

[1]Department of Connectomics, Max Planck Institute for Brain Research, D-60438 Frankfurt, Germany

[2]Probabilistic Numerics Group, Max Planck Institute for Intelligent Systems, D-72076 Tübingen, Germany

* equally contributing first authors

Correspondence: mh@brain.mpg.de

ABSTRACT

The dense circuit structure of the mammalian cerebral cortex is still unknown. With developments in 3-dimensional (3D) electron microscopy, the imaging of sizeable volumes of neuropil has become possible, but dense reconstruction of connectomes from such image data is the limiting step. Here, we report the dense reconstruction of a volume of about 500,000 μm^3 from layer 4 of mouse barrel cortex, about 300 times larger than previous dense reconstructions from the mammalian cerebral cortex. Using a novel reconstruction technique, FocusEM, we were able to reconstruct a total of 0.9 meters of dendrites and about 1.8 meters of axons investing only about 4,000 human work hours, about 10-25 times more efficient than previous dense circuit reconstructions. We find that connectomic data alone allows the definition of inhibitory axon types that show established principles of synaptic specificity for subcellular postsynaptic compartments. We find that also a fraction of excitatory axons exhibit such subcellular target specificity. Only about 35% of inhibitory and 55% of excitatory synaptic subcellular innervation can be predicted from the geometrical availability of membrane surface, revoking coarser models of random wiring for synaptic connections in cortical layer 4. We furthermore find evidence for enhanced variability of synaptic input composition between neurons at the level of primary dendrites in cortical layer 4. Finally, we obtain evidence for Hebbian synaptic weight adaptation in at least 24% of connections; at least 35% of connections show no sign of such previous plasticity. Together, these results establish an approach to connectomic phenotyping of local dense neuronal circuitry in the mammalian cortex.

INTRODUCTION

The cerebral cortex of mammals houses an enormously complex intercellular interaction network implemented via neuronal processes that are long and thin, branching, and extremely densely packed. Early estimates reported an expected 4 kilometers of axons and 400 meters of dendrites compressed into a cubic millimeter of cortical tissue (Braitenberg and Schüz, 1998). This high packing density of cellular processes has made the locally dense mapping of neuronal networks in the cerebral cortex challenging.

So far, reconstructions of cortical tissue have been either sparse (e.g., (da Costa and Martin, 2009; Han et al., 2018; Lee et al., 2016; Lubke et al., 2003; Oberlaender et al., 2011; Schmidt et al., 2017) or restricted to small volumes of about 1500 μm^3 (Kasthuri et al., 2015). Consequently the detailed network architecture of the cerebral cortex is unknown; in particular the question to what degree local neuronal circuits are explainable by geometric rules alone, or whether neurons exhibit innervation specificities beyond such geometric preferences is still debated (Kasthuri et al., 2015; Ko et al., 2011; Lee et al., 2016; Markram et al., 2015; Mischenko et al., 2010). Here we report a dense reconstruction of local cortical tissue sized about 500,000 μm^3, i.e. about 300 times larger than previous dense cortical reconstructions (Kasthuri et al., 2015).

We developed a dense reconstruction method, FocusEM, to obtain the reconstruction of about 2.7 meters of neurite (1.8 meters of axons and about 0.9 meters of dendrites) with an investment of about 4,000 human work hours. When compared to previous dense connectomic reconstructions, this constitutes an advance of about 10-fold (compared to dense reconstructions in the fly larva, (Eichler et al., 2017)), about 20-fold (cf. mouse retina (Helmstaedter et al., 2013)) and about 25-fold (cf. mouse cortex (Kasthuri et al., 2015)).

When analyzing the connectivity between 6,979 axons and 3,719 postsynaptic neurites in this tissue, we find that at least about 58% of inhibitory and about 24% of excitatory axons show specificity for synaptic targets such as cell bodies, apical dendrites and axon initial segments. We determine that only about 35-55% of this synaptic specificity can be deduced from the geometrical arrangement of axons and dendrites alone at scales typically employed for statistical connectivity prediction

3

77   (Lubke et al., 2003; Meyer et al., 2010; Oberlaender et al., 2012a), establishing an

78   upper bound on the geometrical explainability of synaptic innervation in cortical

79   tissue. Furthermore, we find that the thalamocortical synaptic input distributions of

80   dendrites are configured to yield enhanced variability. Finally, a fraction of excitatory

81   axons show synaptic size similarity that is consistent with Hebbian plasticity, which at

82   the same time can be ruled out for about 35% of the circuit. With this we uncover

83   rules of wiring and synaptic specialization in the cerebral cortex and provide a

84   methodology for connectomic screening of cortical tissue.

85

RESULTS

We acquired a 3-dimensional EM dataset from a 28 day old mouse from layer 4 of primary somatosensory cortex (Fig. 1a-d) using serial block-face electron microscopy (SBEM, (Denk and Horstmann, 2004)). The dataset had a size of 61.8 x 94.8 x 92.6 μm^3 and a voxel size of 11.24 x 11.24 x 28 nm^3. We 3D-aligned the acquired images for manual annotation (webKnossos (Boergens et al., 2017)) and automated analysis. We first detected blood vessels and cell bodies using automated heuristics (Fig. 1e), followed by reconstruction of the remaining image volume using machine-learning-based image segmentation (SegEM, (Berning et al., 2015)). The result of this processing were 15 million volume segments corresponding to pieces of axons, dendrites and somata (volume: 0.0295 ± 0.3846 μm^3; mean ± std.). We then constructed the neighborhood graph between all these volume segments and computed the properties of interfaces between directly adjacent volume segments. Based on these features (see Methods), we trained a connectivity classifier to determine whether two segments should be connected (along an axon or a dendrite or a glial cell) or whether they should be disconnected (Fig. 1f). Using the SynEM classifier (Staffler et al., 2017), we determined whether an interface between two disconnected processes corresponded to a chemical synapse, and if so, which was the pre- and which the postsynaptic neurite segment. We furthermore trained a set of classifiers to compute for each volume segment the probability to be part of an axon, a dendrite, a spine head or a glia cell (Fig. 1f-g, precision and recall were 91.8%, 92.9% for axons, 95.3%, 90.7% for dendrites, 97.2%, 85.9% for astrocytes, and 92.6%, 94.4% for spine heads, respectively).

Cell body-based neuron reconstruction

First, we reconstructed those neurons, which had their cell bodies in the tissue volume (Fig. 1h,i, Supplementary Material 1, n=125 cell bodies, of these 97 neuronal, of these 89 reconstructed with dendrites in the dataset) using a set of simple growth rules for automatically connecting neurite pieces based on the segment-to-segment neighborhood graph and the connectivity and neurite type classifiers (Fig. 1f, see Methods). As a result, we obtained fully automated reconstructions of the neuron's soma and dendritic processes. Notably with a minimal additional manual correction investment of 9.7 hours for 89 cells (54.5 mm

118 dendritic and 2.1 mm axonal path length), the dendritic shafts of these neurons could
119 be reconstructed without merge errors, but 37 remaining split errors, at 87.3%
120 dendritic length recall (Fig. 1h,i, Supplementary Material 1, see Methods). This
121 reconstruction efficiency compares favorably to recent reports of automated
122 segmentation of neurons in 3D EM data from the bird brain obtained at about 2-fold
123 higher imaging resolution (Januszewski et al., 2018), which reports soma-based
124 neuron reconstruction at an error rate of beyond 100 errors per 66 mm dendritic
125 shafts at lower (68%) dendritic length recall, with a similar resource investment (see
126 Methods).

127 In addition to the dendritic shafts, the dendritic spines constitute a major fraction of
128 the dendritic path length in cortical neuropil (Fig. 1j). Using our spine head classifier,
129 we found 415,797 spine heads in the tissue volume i. e. density of 0.784 per μm^3
130 (0.98 per μm^3 of neuropil, when excluding somata and blood vessels). In order to
131 connect these to the corresponding dendritic shafts we trained a spine neck
132 continuity algorithm that was able to automatically attach 58.9% of these spines
133 (evaluated in the center of the dataset, at least 10 μm from the dataset border)
134 yielding a dendritic spine density of 0.672 per μm dendritic shaft length (comparable
135 to spine densities in the bird brain, (Kornfeld et al., 2017)). However in mammals, the
136 density of spines along dendrites is even higher (about 1 μm^{-1}). The remaining spine
137 heads were then attached to their dendritic shafts by seeding manual reconstructions
138 at the spine heads and asking annotators to continue along the spine necks to the
139 dendritic shafts. This consumed an additional 900 hours of human work for the
140 attachment of 98,221 spines, resulting in a final spine density of 0.959 per μm
141 dendritic shaft length.

142 **Dense tissue reconstruction**

143 The reconstruction of neurons starting from their cell bodies was however not the
144 main challenge. Rather, the remaining processes, that is axons and dendrites not
145 connected to a cell body within the dataset and densely packed in the tissue,
146 constitute about 97% of the total neuronal path length in this volume of cortex (Fig.
147 1j). To reconstruct this vast majority of neurites (Fig. 1k,l), we first used our
148 connectivity and neurite type classifiers to combine neurite pieces into larger
149 dendritic and axonal agglomerates (see Methods). Then, we took those

6

150 agglomerates that had a length of at least 5 μm (n=74,074 axon agglomerates),
151 detected their endings that were not at the dataset border and directed focused
152 human annotation to these endings ("queries", Fig. 1m,n). For human annotation, we
153 used an egocentric directed 3D image data view ("flight mode" in webKnossos),
154 which we had previously found to provide maximized human reconstruction speed
155 along axons and dendrites in cortex (Boergens et al., 2017). Here, however, instead
156 of asking human annotators to reconstruct entire dendrites or axons, we only queried
157 their judgement at the endings of automatically reconstructed neurite parts. To make
158 these queries efficient, we made three additions to webKnossos: We oriented the
159 user along the estimated direction of the neurite at its ending, reducing the time the
160 user needs to orient within the 3D brain tissue; we dynamically stopped the user's
161 flight along the axon or dendrite whenever another of the already reconstructed
162 neurite agglomerates had been reached; and we pre-loaded the next query while the
163 user was annotating (Fig. 1m,n). With this, the average user interaction time was
164 21.3 ± 36.1 s per query, corresponding to an average of 5.5 ± 8.8 μm traveled per
165 query. In total, 242,271 axon ending queries consumed 1,978 paid out work hours
166 (i.e. including all overheads, 29.4 s per query).

167 However, we had to account for a second kind of reconstruction error, so-called
168 mergers, which can originate from the original segmentation, the agglomeration
169 procedure, or erroneous flight paths from human queries (Fig. 1o). In order to detect
170 such mergers, we started with the notion that most of these merger locations will
171 yield a peculiar geometrical arrangement of a 4-fold neurite intersection once all
172 neurite breaks have been corrected ("chiasma", Fig. 1o). Since such chiasmatic
173 configurations occur rarely in branching neurites, we directed human focused
174 annotation to these locations. First, we automatically detected these chiasmatic
175 locations using a simple heuristic to detect locations at which axon-centered spheres
176 intersected more than three times with the axon (Fig. 1o, n=55,161 chiasmata; for
177 approaches to detect such locations by machine learning, see (Rolnick and Shavit,
178 2017; Zung et al., 2017)). Then, we positioned the user queries at a certain distance
179 from the chiasma location, pointing inward (Fig. 1o) and then used a set of case
180 distinctions to query a given chiasma until its configuration had been resolved (see
181 Methods for details). Chiasma annotation consumed an additional 1,132 work hours
182 (note that the detection of endings and chiasmata was iterated 8 times for axons,

183   see Methods, and that in a final step we also detected and queried 3-fold neurite

184   configurations to remove remaining mergers). With this we obtained in summary a

185   reconstruction of 2.72 meters of neuronal processes (Fig. 1p, 0.89 meters of

186   dendrites (including 0.55 meters of spine necks) and 1.76 meters of axons) with a

187   total investment of 3,981 human work hours – about 10 times faster than a recent

188   dense reconstruction in the fly larval brain ((Eichler et al., 2017), Fig. 1q), about 20

189   times faster than the previous dense reconstruction from the mammalian retina

190   ((Helmstaedter et al., 2013)), and about 25 times faster than the previous dense

191   reconstruction from mammalian cortex (Kasthuri et al., 2015).

192   We then measured the remaining reconstruction error rates in this dense neuropil

193   reconstruction. Since the following of neurites in dense neuropil is much more

194   difficult than the reconstruction of dendrites and proximal axons from the cell body

195   (Fig. 1h,i) we expected this error rate to be substantially higher. In fact, when we

196   quantified the remaining errors in a set of 10 randomly chosen axons we found 12.8

197   errors per millimeter of path length (of these 8.7 per millimeter continuity errors, see

198   Methods). This is indistinguishable from the error rates previously found in fast

199   human annotations (Boergens et al., 2017; Helmstaedter et al., 2011; Helmstaedter

200   et al., 2013).

201   **Connectome Reconstruction**

202   Given the reconstructed pre- and postsynaptic neurites in the tissue volume, we then

203   went on to extract their connectome. For this we used SynEM (Staffler et al., 2017)

204   to detect synapses between the axonal presynaptic processes and the postsynaptic

205   neurites (for non-spine synapses, improvements to SynEM were made to enhance

206   precision and recall, see Methods). Since we were interested in analyzing the

207   subcellular specificity of neuronal innervation, we had to also classify which of the

208   post-synaptic membranes belong to cell bodies; to classify spiny dendrites as

209   belonging to excitatory cells, smooth dendrites belonging to interneurons; and to

210   detect axon initial segments and those dendrites that were likely apical dendrites of

211   neurons located in deeper cortical layers. We developed semi-automated heuristics

212   to detect these subcellular compartments (Fig. 2a-d, see Methods for details).

213   With this we obtained a connectome between 34,221 pre-synaptic axonal processes

214   and a total of 11,400 post-synaptic processes (i. e. somata, axon initial segments

8

215   and dendrites). Restricting the connectome to those pre- and postsynaptic neurites

216   that established at least 10 synapses each yielded a 6,979 by 3,719 connectivity

217   matrix, reporting the number of synapses established between each pair of pre- and

218   postsynaptic neurites (Fig. 2e). The postsynaptic processes comprised 80 somata,

219   246 smooth dendrites, 169 apical dendrites, and 116 axon initial segments (Fig. 2e,

220   for AIS also those with less than 10 input synapses are shown). The dendrites of

221   soma-based neuron reconstructions were labeled as proximal dendrites. In addition,

222   we automatically determined for each synapse whether it was established onto a

223   spine head, dendritic shaft or soma.

Synaptic specificity

225   Then we investigated whether based solely on connectomic information (Fig. 2) we

226   could extract the rules of subcellular innervation specificity described for inhibitory

227   axons in the mammalian cortex (for a review see (Kubota et al., 2016)), and whether

228   such synaptic specificity could also be found for excitatory axons. We first measured

229   the preference of each axon for innervating dendritic spine heads versus dendritic

230   shafts and other targets (Fig. 3a,b). In the mammalian brain, most axons of inhibitory

231   interneurons preferentially innervate the dendrites' shafts or neuronal somata (see

232   e.g. (Kubota et al., 2016)), and most excitatory glutamatergic axons preferentially

233   innervate the spine heads of dendrites (Feldmeyer et al., 2002; Shepherd and Harris,

234   1998). Accordingly, in our dense data, we found that the fraction of primary spine

235   synapses per axon (out of all synapses of that axon) has a clear peak at about 80%

236   (Fig. 3a,b), allowing the identification of spine-preferring, likely excitatory axons with

237   at least 50% primary spine innervations. Similarly, we identified shaft-preferring,

238   likely inhibitory axons with less than 20% primary spine innervations. Together this

239   yielded 6,449 axons with clear shaft or spine preferences. For the remaining n=528

240   axons with primary spine innervations above 20% and below 50%, we first wanted to

241   exclude remaining mergers between excitatory and inhibitory axons (that would yield

242   intermediate spine innervation rates) and split these axons at possible merger

243   locations (at least 3-fold intersections). Of these, 338 now had at least 10 synapses

244   and spine innervation rates below 20% or above 50%. The remaining n=192 axons

245   (2.75% of all axons with at least 10 synapses) were not included in the following

246   analyses. This together yielded n=5,894 excitatory and n=893 inhibitory axons in our

247   data.

9

248   Previous reports have described that a subset of excitatory axons in cortical L4

249   preferentially target the shafts of dendrites in some species (Lubke et al., 2000;

250   McGuire et al., 1984): a study of L4 spiny neurons' axons in juvenile rat found

251   preferential innervation of small-caliber dendritic shafts (and only 27% of synapses

252   onto spines, (Lubke et al., 2000)), and in cat visual cortex, a subset of corticocortical

253   excitatory axons from layer 6 has been described to establish preferentially shaft

254   synapses onto spiny dendrites in L4 at the end of short axonal branches, yielding

255   boutons terminaux (Ahmed et al., 1994; McGuire et al., 1984)). To check whether

256   these axons would confound our assignment of shaft-preferring axons as inhibitory,

257   we randomly selected 20 shaft synapses onto spiny dendrites and manually

258   reconstructed the presynaptic axons with their output synapses. We first asked

259   whether any of these axons would preferentially establish boutons terminaux onto

260   shafts, as described in cat, but found no such axon, indicating that this innervation

261   phenotype comprises less than 5% or is absent in our data from mouse L4 (compare

262   to the estimate of more than 40% of such inputs in cat L4 (Ahmed et al., 1994)). We

263   then checked whether any of the 20 axons showed both a preference for shaft

264   innervation and in a minority of cases any clear primary spine head innervation, as

265   described for the L4 axons in juvenile rat. We found no such example, indicating that

266   none of the shaft-preferring axons was excitatory. This is consistent with data from

267   cat which suggested that L4 spiny axons preferentially target spines (Ahmed et al.,

268   1994). Together, we conclude that in our data from mouse L4, excitatory axons

269   preferentially establish primary spine head innervations (Fig. 3b) and inhibitory axons

270   preferentially innervate the shafts of dendrites.

271   Within cortical layer 4, the two main types of excitatory synaptic input are afferents

272   from the thalamus (thalamocortical inputs, TC) and intracortical inputs

273   (corticocortical, CC). In order to distinguish between corticocortical and

274   thalamocortical excitatory axons (Fig. 3c-f), we used previously established criteria

275   about the frequency of multi-target boutons, bouton size and the number of targets

276   per bouton that had been shown to identify TC inputs in layer 4 of mouse S1 cortex

277   ((Bopp et al., 2017); Fig. 3c-f, see Methods). Using these, we extracted the likely

278   thalamocortical (TC) axons (Fig. 3e,f; n = 569, 9.7% of excitatory axons).

279   We then determined for each of the subcellular synaptic target classes (somata

280   (SOM), axon initial segments (AIS), apical dendrites (AD), smooth dendrites (SD),

281   proximal dendrites (PD), see Fig. 2 and Fig. 3g) the per-synapse innervation

282   probability that would best explain whether an inhibitory axon establishes at least

283   one synapse onto each of these targets (these inhibitory "first-hit" binomial

284   innervation probabilities were 4.2% (SOM), 17.8% (PD), 4.9% (SD), 3.3% (AD), and

285   0.5% (AIS), see Methods, Fig. 3h). We then computed the expected distribution of

286   synapses per axon made onto each target class assuming the second-hit, third-hit,

287   etc. innervation probabilities are the same as the probability to establish at least one

288   synapse onto that target. When comparing these target distributions to the actually

289   measured distributions of synapses per axon onto each target class (Fig. 3i), we

290   found that inhibitory axons established enhanced specificity for cell bodies

291   ($p=2.4 \times 10^{-34}$, n=893, one-sided Kolmogorov-Smirnov test), proximal dendrites

292   ($p=6.0 \times 10^{-77}$), apical dendrites ($p=2.5 \times 10^{-4}$) and smooth dendrites ($p=1.7 \times 10^{-3}$), but

293   no enhanced specificity for axon initial segments in L4 (p=0.648, note that AIS are

294   synaptically innervated by 0.172 input synapses per μm AIS length; but these

295   innervations are not made by certain axons specifically, unlike in supragranular

296   layers (Taniguchi et al., 2013)).

297   When performing the same analysis for excitatory axons (Fig. 3j), we found clear

298   target specificity for apical dendrites ($p=2.5 \times 10^{-34}$, Fig. 3j), for smooth dendrites

299   ($p=7.6 \times 10^{-25}$) and for proximal dendrites ($p=1.3 \times 10^{-169}$). Thalamocortical axons, to

300   the contrary, show indication of target specificity for proximal dendrites ($p=2.5 \times 10^{-31}$),

301   but not for apical (p=0.019) or smooth dendrites (p=0.723).

302   These results provide statistical connectomic evidence for the existence of target-

303   specific wiring of inhibitory and excitatory axons in cortical layer 4. Next, we wanted

304   to determine the fraction of inhibitory and excitatory axons that had an unexpectedly

305   high synaptic preference for one (or multiple) of the subcellular target classes. For

306   this, we determined for each axon the probability that its particular synaptic target

307   choices had originated from a simple chance drawing given the first-hit probabilities

308   (Fig. 3h), or whether it showed additional specificity. Here, we used the false

309   detection rate criterion used for the determination of significantly expressed genes (q

310   value, (Storey and Tibshirani, 2003), see Methods). As a result, we obtained lower

311   bounds on the fractions of axons in the tissue that are specifically innervating the

312   various subcellular target classes (Fig. 3k; 58.0% of inhibitory and 24.4% of

313   excitatory axons). Of those inhibitory axons found to be target-specific, about 83% of

11

314 axons are specific for somata or proximal dendrites, about 14% for apical dendrites,
315 and about 3% for the smooth dendrites of other interneurons. Interestingly, we also
316 found subsets of excitatory axons with subcellular target specificity: of those
317 excitatory axons with significant synaptic target specificity, about 28% are specific for
318 apical dendrites and about 14% for smooth dendrites. Furthermore, at least 24.7% of
319 thalamocortical axons specifically innervated proximal dendrites (Fig. 3k).

320 Finally, we asked whether the specificity of axons towards one particular synaptic
321 target yields an enhanced (or suppressed) innervation of other synaptic targets (i.e.,
322 whether axons exhibit conditional, higher-order synaptic specificity, Fig. 3l,m). For
323 example, given axons that show enhanced innervation of somata, would the target
324 distribution of the non-somatic synapses of these axons be random, or would these
325 remaining synapses show additional target preferences or target suppression (Fig.
326 3l,m)? For this, we analyzed all axons of certain target specificity as identified before
327 (Fig. 3k), excluded synapses of these axons onto their specifically innervated target,
328 measured the fractions of remaining synapses onto the other target classes and
329 compared them to the average innervation rate over all axons (Fig. 3l,m). We found
330 that inhibitory axon subpopulations with soma- and proximal dendrite-specificity are
331 overlapping, and axons with specificity towards apical and smooth dendrites exhibit
332 suppressed innervation of the proximal dendritic/somatic targets and vice versa (Fig.
333 3l). Excitatory axons show only very weak conditional innervation preference (Fig.
334 3m).

335 Together these results represent the patterns of subcellular synaptic innervation
336 rules exhibited in a local cortical circuit in layer 4. It should be noted that the
337 definition of presynaptic axonal types was performed relying only on connectomic
338 data; not on expression markers or cell morphology. Such a cell type classification
339 based on local connectomic data alone has been successful in the mammalian retina
340 before (connectomic definition of a third subtype of type 5 bipolar cells (Helmstaedter
341 et al., 2013)) – but whether it would be possible in dense mammalian cortical data
342 was not clear *a-priori*. The fact that the connectomically defined axonal classes
343 exhibit additional higher-order innervation preference (Fig. 3l) further indicates that
344 these are in fact valid axonal type definitions.

345

Geometric explainability of synaptic innervations

346 We were now able to ask whether these local connectivity rules (Fig. 3) could have

347 been derived solely from the geometry of axons and dendrites. The question to what

348 degree the trajectories of axons and dendrites are already predictive of synaptic

349 innervation in the cerebral cortex has been controversially debated (Binzegger et al.,

350 2004; Braitenberg and Schüz, 1998; Kasthuri et al., 2015; Lee et al., 2016; Markram

351 et al., 2015), and an assumption of random innervation has been put forward

352 (Peters' rule, (Braitenberg and Schüz, 1998)) and used for massive simulation

353 initiatives (Markram et al., 2015). While connectomic examples of non-random

354 innervation in the cortex are documented (da Costa and Martin, 2009; Kasthuri et al.,

355 2015; Mishchenko et al., 2010; Schmidt et al., 2017), a rigorous analysis within

356 dense cortical neuropil of sufficient scale is missing.

357 We first compared the fraction of synapses made onto the subcellular target classes

358 with the fraction of membrane surface attributed to these subcellular domains,

359 sampled in cubes of ~5 µm edge length within the dataset volume (Fig. 4a). The

360 membrane surface fraction deviated up to a factor of 2 from the actual synapse

361 fraction, both underestimating (apical dendrites, Fig. 4a) and overestimating

362 (somata) the synaptic innervation.

363 We then investigated whether the postsynaptic membrane surface available within a

364 certain radius r_{pred} around a given axon (Fig. 4b,c) would be a better predictor of

365 synaptic innervation for that given axon. For this we measured the available

366 membrane surface belonging to the 5 subcellular target classes around all axons

367 (Fig. 4d).

369 We then used a logistic multinomial regression model to predict synaptic innervation

370 from the availability of membrane surface attributed to the target classes around the

371 6,979 axons (Fig. 4e). In this we assumed that the precise axonal trajectories were

372 known (corresponding to perfect alignment of axonal and dendritic reconstructions),

373 and that the number of synapses per axon was given. Based on this, we computed

374 the coefficient of determination (R^2) reporting the fraction of axonal synaptic

375 innervation variance that could be explained purely based on the geometrical

376 information (Fig. 4f). For this we subtracted the variance originating from the

377 multinomial sampling of a concrete innervation target per synapse and axon (see

13

378   Methods), thus reducing the variance that has to be explained by the geometric

379   model. Yet, even using these favorable conditions, at a prediction radius of 10 μm,

380   only up to 41% of inhibitory innervation and about 54% of excitatory innervation

381   variance was accounted for by the geometric model (Fig. 4f). This lack of

382   geometrical predictability was present for all types of axons (Fig. 4f). Notably,

383   commonly used integration scales for geometrical connectomic prediction (25 μm,

384   (Binzegger et al., 2004; Lubke et al., 2003; Meyer et al., 2010; Oberlaender et al.,

385   2012a)) provided only about 34% explained variance of actual synaptic innervation

386   for inhibitory and only about 50% for excitatory axons under the rather optimal

387   predictive conditions as described above.

Dendritic and axonal synapse positioning

389   We next investigated the distribution of input and output synapses along the soma,

390   dendrites and axons of the excitatory L4 neurons (Fig. 5). Up to about 20 μm from

391   the soma, almost no spines are established (Fig. 5a). While the total number of

392   excitatory synapses increases substantially until about 50 μm from the soma, the

393   fraction of excitatory input contributed by TC axons stays remarkably constant at

394   about 12% from 20 μm onwards (Fig. 5b). The inhibitory-excitatory synaptic input

395   ratio (i/(i+e)) drops from almost 100% to about 15% within 50 μm, and further

396   decreases to about 7% at 100 μm from the soma (Fig. 5b).

397   To study the positioning of synapses along excitatory axons, we used those axons

398   leaving the cell bodies to ask whether synapses were sorted along the axonal path

399   according to their target (Fig. 5c,d). While target-sorted placement of output

400   synapses along axons had been theoretically predicted and found in non-mammalian

401   species (Carr and Konishi, 1988, 1990; Jeffress, 1948; Kornfeld et al., 2017), the

402   discovery of sorted synaptic arrangements along axons in layer 2 of the mammalian

403   medial entorhinal cortex was a surprise (Schmidt et al., 2017). Here, we found no

404   evidence for path-length dependent axonal synapse sorting (PLASS) in layer 4 of

405   mouse somatosensory cortex (Fig. 5d), excluding PLASS as a ubiquitous cortical

406   wiring principle, but leaving open the possibility that it could be a feature of non-

407   granular cortex.

408

14

Synaptic input variability

Functional recordings of cortical neurons *in-vivo* show a remarkable variability of responses between neurons but also between stimulus exposures for a given neuron (Brecht and Sakmann, 2002; Kerr et al., 2007; Kerr et al., 2005; Ohki et al., 2005; Stosiek et al., 2003). A heterogeneous sampling of available synaptic inputs at the level of neurons and dendrites equipped with non-linear functional properties (Lavzin et al., 2012) could be one mechanism generating such variable functional responses. Using our dense synaptic input data, we wanted to next analyze the variability of synaptic input composition in L4 neurons (Fig. 5e-n).

We first noticed that the density of thalamocortical synapses had a substantial dependence on cortex depth (Fig. 5e-h): the absolute density of TC synapses in the volume increased by about 93% over 50 µm cortex depth (Fig. 5e,f; the TC excitatory synapse fraction TC/(TC+CC) increased by 82.6%, corresponding to an absolute increase in the TC synapse fraction of 5.8% per 50 µm cortex depth, Fig. 5h). This gradient is consistent with light-microscopic analyses of TC synapses showing a decrease of TC synapse density from lower to upper L4 (Garcia-Marin et al., 2013; Oberlaender et al., 2012b; Wimmer et al., 2010) which is most substantial when analyzed at the level of single VPM axons (Oberlaender et al., 2012b). Neither the inhibitory nor the corticocortical synapse densities showed a comparable spatial profile (Fig. 5g).

We wanted to understand how the synaptic TC gradient is mapped onto the input of L4 neurons along the cortex axis (Fig. 5i-k). One possibility was that the TC synapse gradient (Fig 5e,f,h) is used to enhance the variability of synaptic input composition between different primary dendrites of the L4 neurons such that a neuron's dendrites pointing upwards towards the pia would sample relatively less TC input than dendrites pointing towards the white matter. Alternatively, synaptic specificity mechanisms (as in Fig. 3) could be used to counterbalance this synaptic gradient and equilibrate the synaptic input fractions on the differently oriented dendrites. Our analysis (Fig. 5j,k) shows that in fact, even for single primary dendrites, TC input fractions vary 1.28-fold between dendrites pointing upwards towards the cortical surface vs downwards towards the white matter (TC input fractions of each dendrite were corrected for the entire neuron's TC input fraction for this analysis, see

15

441   Methods). This finding of per-dendrite input variation points to a circuit configuration

442   in which TC input variability is enhanced between and within neurons of the same

443   excitatory type in cortical layer 4.

444   The finding of a substantial TC synapse gradient along the cortical axis within L4 is

445   interesting, since the fractional thalamocortical innervation of spiny neurons in L4

446   has been a matter of extensive scientific investigation (Ahmed et al., 1994;

447   Benshalom and White, 1986; Bopp et al., 2017; da Costa and Martin, 2009; Garcia-

448   Marin et al., 2017; Latawiec et al., 2000; White, 1989; White and Hersch, 1981), with

449   results of TC input fraction ranging from less than 10% (da Costa and Martin, 2009)

450   to up to 20% (Benshalom and White, 1986; White, 1989) of synaptic excitatory input

451   contributed from the thalamus in layer 4 of sensory cortex. While most differences

452   have so far been attributed to species differences (Bopp et al., 2017), our data

453   supports the view that cortical depth within layer 4 may be a key determinant of TC

454   input fraction (Garcia-Marin et al., 2017). Our data also emphasizes the

455   heterogeneity of synaptic input for cortical neurons of similar type.

Connectomic signature of synaptic plasticity

457   Finally we used the unprecedented magnitude of synaptically coupled axons and

458   dendrites in this dense cortical volume to look for a potential connectomic signature

459   of previous episodes of synaptic plasticity. In one well-established concept of

460   neuronal plasticity, the timing of action potentials in pre- and postsynaptic neurons is

461   the key determinant of synaptic weight change (Hebb, 1949; Markram et al., 1997).

462   Since synaptic strength has been shown to be correlated to the size of synaptic

463   specializations (postsynaptic density, spine head volume, (Harris and Stevens, 1988,

464   1989) and axon-spine interface (ASI) area (de Vivo et al., 2017)), the analysis of the

465   similarity of synaptic size for pairs of pre- and postsynaptic neurites that establish

466   more than one joint synapse can be used to obtain evidence for previous episodes of

467   synaptic weight assimilation between these joint synapses. In the hippocampus,

468   where activity-dependent synaptic weight increase is consistently found (LTP), this

469   argument has been employed to investigate the storage capacity of synapses (Bartol

470   et al., 2015; Bromer et al., 2018), and joint-synapse size homogeneity has been

471   described for clustered synaptic input (Bloss et al., 2018). Here, we wanted to

472   determine whether such synaptic size homogenization can be quantitatively

16

473 determined in cortical layer 4, in which only long-term synaptic depression has been

474 found (Egger et al., 1999), and to determine upper and lower bounds on the fraction

475 of the circuit that can have recently undergone such synaptic weight adaptation.

476 For this, we first searched for all pairs of axons and dendrites that established more

477 than one joint axon-to-spine synapse in the volume (Fig. 6a-c, n=6,602; of these

478 n=6,045 with 2, n=474 with 3, and n=83 with 4 and more synapses; we call them

479 joint synapses in the following; this analysis was carried out both in the original axon

480 reconstruction and in a reconstruction with all axons split at potential branch points

481 and merger points; the latter served as control for the influence of merge errors on

482 the results; in both cases the reported effects were found; the reported numbers are

483 from the control case). We then measured the size of the axon-spine interface (ASI,

484 (de Vivo et al., 2017; Staffler et al., 2017)) for all synapses, those with 2 joint

485 synapses, etc. (Fig. 6d). Surprisingly, mean synaptic size increased by 1.15-fold per

486 additional joint synapse. Given the absence of electrophysiological evidence for LTP

487 in L4 (Egger et al., 1999), this finding could correspond to the subset of extremely

488 strong unitary synaptic connections in L4 reported by (Feldmeyer et al., 1999) which

489 had a unitary synaptic efficacy of up to 10 mV, allowing to elicit postsynaptic APs

490 based on one synaptically connected presynaptic neuron. Alternatively, this data

491 could indicate that in a subset of the L4 circuit, LTP is established. In this case, our

492 data would support a model in which additional synapses are added when previous

493 coincident pre- and postsynaptic activity has already strengthened the existing joint

494 synapses. This could also indicate that the more joint synapses are established

495 between LTP-enabled connections, the more likely it is that the single presynaptic

496 axon elicits APs in the postsynaptic neuron, enhancing possible synapse strength

497 increase – and giving rise to the reported extremely large unitary connections

498 (Feldmeyer et al., 1999).

499 We then measured the coefficient of variation (CV) of the axon-spine interface (ASI)

500 area for random pairs of spine synapses (CV = 0.50 ± 0.32, mean ± s.d., n = 70,202)

501 (Fig. 6e), for pairs of spine synapses sampled from the same dendrite but different

502 input axons (CV = 0.50 ± 0.32; n = 64,934; indistinguishable from the random case,

503 p = 0.07, one-sided Kolmogorov-Smirnov test), pairs of spine synapses sampled

504 from the same axon but different target dendrites (CV = 0.49 ± 0.32; n = 54,256;

505 slightly different from the random case, p = 1.7×10^{-8}), and finally joint synapses

506   established by the same axon onto the same dendrite (CV = 0.44 ± 0.30; n = 6,045;

507   substantially smaller than the random case, p = 1.4×10^{-40}). This data indicates that

508   while heteronomous combinations of synapse pairs follow the random synapse pair

509   distribution (Fig. 6e), for joint synapse pairs, significantly more pairs have

510   substantially less synaptic variance (CV < 0.54) and substantially less pairs are

511   found with a CV > 0.54. This data implies an excess of n=538 low-CV synapse pairs

512   (i.e. 8.9%) compared to the random case (Fig. 6e), suggesting synapse pairs with a

513   CV<0.54 as those that have been exposed to processes that homogenize synapse

514   size. At least 35.1% (n=2,122) of connections involved in joint synapses show

515   however a CV>0.54 that precludes such previous synapse size homogenization.

516   We next investigated the relationship between synapse size and its variability for

517   joint synapse pairs, asking whether both the reduced size variability (Fig. 6e) and the

518   average increase in joint synapse size (Fig. 6d) are caused by the same joint

519   synapse pairs. For this we obtained the distribution of synapse size and its variability

520   for all pairs of joint synapses (Fig. 6f) and subtracted a similar distribution randomly

521   drawn from the size distribution of all (coupled and uncoupled) synapses (Fig. 6g).

522   The resulting data clearly shows that reduced synapse size variability and increased

523   synapse size are in fact correlated in the joint synapse pairs (Fig. 6i).

524   We finally wanted to investigate the relation between low-variability synapse pairs

525   and their average size when controlling for the effect that joint synapses have an

526   overall increased average synapse size (Fig. 6d). For this we again took the

527   distribution of synapse size and its variability for all pairs of joint synapses (Fig. 6f),

528   but this time we subtracted a similar distribution randomly drawn from the size

529   distribution of only the joint synapses (Fig. 6h). The resulting data (Fig. 6j) again

530   shows an enrichment of low-CV synapse pairs (Fig. 6j); Surprisingly, however, the

531   data also indicates two separate enriched populations of synapse pairs with low CV:

532   those with low CV and large synapse size (Fig. 6j, upper area, this range of synapse

533   size variability and average synapse size contains 7.9% of all joint synapse pairs),

534   and those with low CV and small synapse size (lower dashed area in Fig. 6j; 15.5%

535   of all synapse pairs in this area).

536   Together, this data provides a connectomic fingerprint of the fraction of synapses in

537   the circuit that have likely experienced previous homogenization of synapse size.

18

538   Both LTD (with saturation of synaptic weight decrease, (Egger et al., 1999)) and LTP

539   are expected to yield such homogenization of synapse size. For at least about 24%

540   of the joint synapse pairs (Fig. 6j), connectomic evidence for synapse size

541   homogenization can be found. For at least about 35% of the joint synapses, however

542   (Fig. 6e), synapse size homogenization cannot have occurred up to about one hour

543   before the connectomic experiment (see (Bartol et al., 2015; Egger et al., 1999) for

544   data on the time scales of synaptic weight change)).

545

DISCUSSION

Using FocusEM, a set of tools for the semi-automated reconstruction of dense neuronal networks in the cerebral cortex, we have obtained the first dense circuit reconstruction from the mammalian cerebral cortex at a scale that allows the analysis of axonal rules of subcellular innervation - about 300 times larger than previous dense reconstructions from cortex (Kasthuri et al., 2015). We find that inhibitory axonal types specifically innervating certain postsynaptic subcellular compartments can be defined solely based on connectomic information (Figs 2,3); that in addition to inhibitory axons a fraction of excitatory axons exhibits such subcellular innervation preferences (Fig. 3); that the geometrical arrangement of axons and dendrites can explain only a moderate fraction of synaptic innervation, revoking random models of cortical wiring (Fig. 4); that a substantial thalamocortical synapse gradient in L4 gives rise to an enhanced heterogeneity of synaptic input composition at the level of single cortical dendrites (Fig. 5); and that the consistency of synapse size between pairs of axons and dendrites signifies fractions of the circuit with and without evidence for synaptic plasticity history, placing an upper bound on the "learned" fraction of the circuit (Fig. 6). Together, FocusEM allows the dense mapping of circuits in the cerebral cortex at a throughput that enables connectomic screening.

Connectomic bounds on error rates

In the development of high-throughput reconstruction techniques for large-scale 3D-EM-based connectomics, the calibration of methodological progress using various definitions of error rates per cable length were initially important (Boergens et al., 2017; Cardona et al., 2012; Helmstaedter et al., 2011; Januszewski et al., 2018). With the ability to obtain dense connectomic maps ((Eichler et al., 2017; Helmstaedter et al., 2013; Wanner et al., 2016a) and this study), methodological proof-of-principle calibration can be replaced by a comparison of actual dense reconstructions and the required resources (Fig. 1p,q).

This becomes advantageous because error rates can be implicitly calibrated by the relevant connectomic analyses for a given dense reconstruction. In the presented data, we determined the required reconstruction accuracy by testing each finding for

20

577 its sensitivity to the remaining reconstruction errors, and by performing manual

578 control reconstructions where necessary (see Methods for details).

579 Once larger EM volumes are to be reconstructed, more investment in error rate

580 reduction may be required (corresponding to higher manual annotation investments)

581 – however, using the extensive labels from dense reconstructions as the present

582 one, future reconstruction approaches may become already more efficient based on

583 this previous knowledge alone.

584 **Connectomic evidence for synaptic plasticity**

585 The extraction of connectomic evidence for synaptic size consistency requires

586 further discussion. While the similarity of synaptic size has been previously used for

587 arguments about synaptic plasticity and learning (Bartol et al., 2015; Bromer et al.,

588 2018), an alternative source of decreased variance of synapse size for defined pairs

589 of axons and dendrites is the establishment of consistently weaker or stronger

590 synaptic connections between certain subtypes of pre- and postsynaptic neurons.

591 While in the L4 circuit, the majority of excitatory connections is known to be

592 established between local spiny neurons, and the observed synaptic size effects

593 (Fig. 6) were also present when excluding TC inputs (data not shown), subtypes of

594 excitatory neurons with different connectivity rules could contribute to the low-

595 variance synaptic size regime. Our result on the lower bound of the fraction of the

596 circuit that has no history of synaptic size homogenization (35%, Fig. 6e), is however

597 unaffected by this cautionary notion.

598 **Outlook**

599 The presented methods and results open the path to the consistent connectomic

600 screening of mammalian tissue from various cortices, layers, species, developmental

601 stages and disease conditions. The fact that even a small piece of mammalian

602 cortical neuropil contains a high density of relevant information, so rich as to allow

603 the extraction of possible connectomic signatures of the "learnedness" of the circuit,

604 makes this approach a promising endeavor for the study of the structural setup of

605 mammalian nervous systems.

21

Competing financial interests:

The authors declare no competing financial interests.

Author contributions:

Conceived, initiated and supervised the project: MH; Performed experiments: KMB; Provided analysis methods: PH; developed and performed analyses: AM, MB, KMB, BS with contributions by all authors; wrote the manuscript: AM, MH with contributions by all authors.

METHODS

Animal experiments

A wild-type (C57BL/6) male mouse was transcardially perfused at postnatal day 28 under isoflurane anesthesia using a solution of 2.5% paraformaldehyde and 1.25% glutaraldehyde (pH 7.4) following the protocol in (Briggman et al., 2011). All procedures followed the animal experiment regulations of the Max Planck Society and were approved by the local animal welfare authorities (Regierungspräsidien Oberbayern and Darmstadt).

Tissue sampling and staining

The fixated brain was removed from the skull after 48h of fixation and sliced coronally using a vibratome. Two samples were extracted using a 1 mm biopsy punch (Integra Miltex, Plainsboro, NJ) from a 1 mm thick slice at 5 mm distance from the front of the brain targeted to layer 4 in somatosensory cortex of the right hemisphere. The corresponding tissue from the left hemisphere was further sliced into 70 μm-thick slices followed by cytochrome oxidase staining indicating the location of the coronal slice to be in barrel cortex.

Afterwards the extracted tissue was stained as in (Briggman et al., 2011). Briefly, the tissue was immersed in a reduced Osmium tetroxide solution (2% OsO_4, 0.15 M CB, 2.5 M KFeCN) followed by a 1% Thiocarbohydrazide step and a 2% OsO_4 step for amplification. After an overnight wash, the sample was further incubated with 1.5% Uranyl Acetate solution and a 0.02 M Lead(II) Nitrate solution. The sample was dehydrated with Propylenoxide and EtOH, embedded in Epon Hard (Serva Electrophoresis GmbH, Germany) and hardened for 48 h at 60 °C.

3D EM experiment

The embedded sample was placed on an aluminium stub and trimmed such that on all four sides of the sample the tissue was directly exposed. The sides of the sample were covered with gold in a sputter coater (Leica Microsystems, Wetzlar, Germany). Then, the sample was placed into a SBEM setup ((Denk and Horstmann, 2004), Magellan scanning electron microscope, FEI Company, Hillsboro, OR, equipped with a custom-built microtome courtesy of W Denk). The sample was oriented so that the

23

665 radial cortex axis was in the cutting plane. The transition between L4 and L5A was

666 identified in overview EM images by the sudden drop in soma density between the

667 two layers (see Fig. 1b). A region of size 96 µm x 64 µm within L4 was selected for

668 imaging using a 3 by 3 image mosaic, a pixel size of 11.24 x 11.24 nm^2, image

669 acquisition rate of 10 MHz, nominal beam current of 3.2 nA (thus a nominal electron

670 dose of 15.8 e$^-$/nm^2), acceleration voltage of 2.5 kV and nominal cutting thickness of

671 28 nm. The effective data rate including overhead time spent during motor

672 movements for cutting and tiling was 0.9 MB/s. 3,420 image planes were acquired,

673 yielding 194 GB of data.

Image alignment

675 After 3D EM dataset acquisition, all images were inspected manually and marked for

676 imaging artifacts caused by debris present on the sample surface during imaging.

677 Images with debris artifacts were replaced by the images at the same mosaic

678 position from the previous or subsequent plane. First, rigid translation-only alignment

679 was performed based on the procedures in (Briggman et al., 2011) which followed

680 closely (Preibisch et al., 2009). The following modifications were applied: When shift

681 vectors were obtained that yielded offsets of more than 100 pixels, these errors were

682 iteratively corrected by manually reducing the weight of the corresponding entry in

683 the least-square relaxation by a factor of 1000 until the highest remaining residual

684 error was less than 10 pixels. Shift calculation of subsequent images in cutting

685 direction was found to be the most reliable measurement and was therefore

686 weighted 3-fold in the weighted least-square relaxation. The resulting shift vectors

687 were applied (shift by integer voxel numbers) and the 3D image data was written in

688 KNOSSOS format (Boergens et al., 2017; Helmstaedter et al., 2011).

Previous usage of 3D image data

690 The 3D EM image dataset using the initial image alignment described above was

691 previously utilized for methods development in (Berning et al., 2015), (Boergens et

692 al., 2017) and (Staffler et al., 2017). Furthermore, reconstructions from this data

693 were used as staining quality comparison in (Hua et al., 2015).

694

695

Subimage alignment

To further improve the precision of image alignment, which we found to critically impact the quality of the automated volume segmentation, we performed the following steps. Each image of the raw dataset was cut into smaller images sized 256x256 pixels each. The offset calculation was run as described above (with the shift between neighboring subimages from the same original image set to zero). Additionally, we used a mask for blood vessels and nuclei (see below) to determine images which mostly contained blood vessels or somata. These images were assigned a decreased weight in the relaxation step. After the least-square relaxation, the shifts obtained for the subimages were used to create a smooth non-affine morphing of the original images, which were then exported to the 3D KNOSSOS format as above. All raw image data will be made available for inspection at demo.webknossos.org (see section on data availability).

Methods description for software code

The following descriptions are aimed at pointing to the key algorithmic steps rather than enumerating all detailed computations.

Blood vessel detection and correction for brightness gradient

Blood vessels were detected (Fig. 1e) by automated identification of regions of at least 0.125 μm^2 with extreme brightness values (below 50 or above 162 at 8 bit depth) in each image plane, followed by manual inspection to exclude false positives. Image voxels within blood vessels were assigned the mean brightness of the entire dataset (mean=121).

To correct brightness gradients across the image volume, the mean brightness was calculated for non-overlapping image blocks of 64 x 64 x 29 vx^3, respectively, and the resulting marginal brightness distributions along the X, Y, and Z axes were smoothed and used to assign a multiplicative correction factor to each image block. The correction factor was linearly interpolated and multiplied to the brightness value of all non-blood vessel voxels within each of the image blocks.

Nuclei and myelin detection

25

725 For the automated detection of nuclei and myelin, the following heuristics were

726 applied. First, the voxel-wise brightness gradient was computed in the image data

727 after smoothing by a 3-D kernel of size 21 x 21 x 9 vx and a standard deviation of

728 ~33.5 nm. Nuclei were identified as regions of at least about 1.8 µm3 size with small

729 brightness gradient and image brightness close to the mean image brightness.

730 Myelin was detected as regions of low brightness sized at least about 0.35 µm3.

731 Both nuclei and myelin detection were applied on overlapping image volumes of 912

732 x 912 x 416 vx^3 size which were then truncated to non-overlapping volumes of 512 x

733 512 x 256 vx^3 size.

Volume segmentation using SegEM

735 To generate an initial automated volume segmentation, SegEM (Berning et al., 2015)

736 was applied to image data cubes of size 1024 x 1024 x 512 vx^3 with 256, 256, and

737 128 vx overlap along X, Y, and Z, respectively, using CNN 20130516T2040408,3

738 with parameters θ_{ms} = 10 vx and θ_{hm} = 0.25 (see Table 1 in (Berning et al., 2015)). At

739 the edge of myelinated regions (see previous section), the CNN output was replaced

740 with the minimum output value of -1.7 to enforce splits during the subsequent

741 watershed-based volume segmentation.

Segmentation neighborhood graph

743 For the determination of neurite continuity and synaptic interfaces (Fig. 1f), a

744 segment neighborhood graph (region adjacency graph) was constructed in each of

745 the non-overlapping segmentation cubes created by the SegEM step (see previous

746 section). The neighborhood graph was constructed as in SynEM (Staffler et al.,

747 2017). Briefly, two volume segments were called adjacent if there was a boundary

748 voxel that contained both segments in its 26-neighborhood. The borders between

749 adjacent segments were calculated as the connected components of all boundary

750 voxels that had both segments in their 26-neighborhood. For each border, an edge

751 between the corresponding segments was added to the neighborhood graph. The

752 segment neighborhood graph is thus an undirected multigraph.

753 To extend the neighborhood graph beyond the non-overlapping segmentation cubes,

754 pairs of segmentation cubes that shared a face in the x, y or z-direction were

755 considered, and segments in the juxtaposed segmentation planes from the two

756 segmentation cubes were matched if the number of matched voxels for a given pair

757 of segments in the two planes was at least 10, and if the matched voxels constituted

758 more than 90% of the area of the smaller segment. In these cases, an edge between

759 the corresponding segments from the neighboring segmentation cubes was added to

760 the neighborhood graph.

Synapse detection with SynEM

762 For synapse detection, SynEM (Staffler et al., 2017) was applied to the segment

763 neighborhood graph (see previous section) as in (Staffler et al., 2017). In brief, for

764 each pair of adjacent volume segments, the subvolumes for SynEM feature

765 aggregation (see (Staffler et al., 2017)) were determined by dilating the border

766 between the two volume segments with spherical structuring elements of radius 40

767 nm, 80 nm and 160 nm, respectively, and then intersecting the dilated border the two

768 adjacent volume segments, each. Interfaces with a border size of less than 151

769 voxels were discarded. Then, all interfaces in the segment neighborhood graph were

770 classified using the SynEM classifier, yielding two SynEM scores for each interface,

771 one for each of the two possible synapse directions.

772 In contrast to (Staffler et al., 2017), separate classifiers for interfaces onto spine

773 segments (retrieved by TypeEM) and for all other interfaces were used. For

774 interfaces onto spine segments, the classifier from (Staffler et al., 2017) was used.

775 All interfaces onto spine segments with at least one score larger than -1.2292

776 according to the SynEM classifier (corresponding to 89% recall and 94% precision

777 for spine synapses; see the test set of (Staffler et al., 2017)) were considered as

778 synaptic interface candidates. For all other interfaces, a second classifier was trained

779 using different training data and a different feature representation of interfaces. The

780 training set of the second classifier consisted of all shaft and soma synapses of the

781 SynEM training set and the shaft and soma synapses from two additional training

782 volumes of size 5.75 x 5.75 x 7.17 μm^3. The feature representation of interfaces for

783 the second classifier consisted of all features of SynEM described in (Staffler et al.,

784 2017), extended by four additional texture filter responses. The additional filter

785 responses were voxel-wise probability maps for synaptic junctions, mitochondria,

786 vesicle clouds and a background class obtained using a multi-class CNN. The CNN

787 was trained on seven volumes of dense annotations for synaptic junctions, vesicle

27

788   clouds and mitochondria (six volumes of size 3.37 x 3.37 x 3.36 μm^3 that were also

789   used for the methods comparison in (Staffler et al., 2017), and one additional volume

790   of size 5.75 x 5.75 x 7.17 μm^3) using the elektroNN framework (elektronn.org; see

791   also (Dorkenwald et al., 2017)). Interfaces onto segments that were not classified as

792   spines by TypeEM with at least one directional SynEM score larger than -1.28317

793   according to the second classifier (corresponding to 69% recall and 91% precision

794   evaluated on all shaft synapses of the test set for inhibitory synapse detection of

795   SynEM; see (Staffler et al., 2017)) were considered as synaptic interface candidates

796   in addition to the synaptic interface candidates onto spines.

797

ConnectEM classifier

799   To determine the continuity between adjacent volume segments (Fig. 1f), for each

800   interface (see previous section) sized at least 10 vx, the SynEM filter bank and

801   aggregation volumes (Staffler et al., 2017) were applied to the image and CNN

802   output data, resulting in 6,426 texture- and 22 shape-features per interface. The

803   features were used as input to an ensemble of 1,500 decision tree stumps trained

804   with LogitBoost (Friedman et al., 2000) on 76,379 labeled edges obtained from

805   proofread dense skeleton annotations of three (5 $\mu m)^3$ cubes of neuropil. To adapt

806   the SynEM interface classification method to a task on undirected edges, the

807   ensemble was trained on both the forward and reverse direction of the labeled

808   edges. Each edge in the segment neighborhood graph was then assigned a

809   continuity probability by applying the classifier to the corresponding interface in

810   random direction. Interfaces with less than 10 vx were treated as having a continuity

811   probability of zero, edges across segmentation cubes were assigned a continuity

812   probability of one.

813

TypeEM classifier

815   To determine whether a volume segment belonged to a dendrite, an axon, or an

816   astrocyte, and whether it was likely a dendritic spine head, we developed a set of

817   four classifiers ("TypeEM") as follows. Each volume segment was expanded into an

818   agglomerate of up to 5 segments by iteratively adding the neighboring segment with

819 the highest edge continuity probability to the agglomerate. Agglomeration was
820 restricted to the subgraph induced by the edges with at least 92% continuity
821 probability to prevent merge errors.

822 Then, the following set of features was computed for the agglomerates: 918 texture
823 features from the SynEM filter bank (Staffler et al., 2017) applied to the image and
824 CNN output data and pooled over the segment agglomerate volume; 6 shape
825 features as in SynEM; the 0th- to 2nd-order statistical moments of the agglomerate
826 volume; the eigendecomposition of the 2nd order statistical moment; the 0th-to-2nd
827 order statistical moments of the surface of the agglomerate after rotation of the
828 agglomerate to the principal component of all its voxels; same as before but for the
829 convex hull of the agglomerate; volume-to-surface area ratio, compactness (i.e.,
830 (surface area)^3 / volume^2), clusters of normal unit vectors, hull crumpliness and
831 packing (Corney et al., 2002); estimates of the distance (Osada et al., 2001) and
832 thickness (Yi et al., 2004) histograms from sampling random point pairs on the
833 agglomerate's surface.

834 This yielded a total of 1,207 shape features and 924 SynEM features; these were
835 then taken as input to an ensemble of 1,500 decision tree stubs trained using
836 LogitBoost (Friedman et al., 2000). 14,657 training samples were obtained by one
837 expert (AM) marking all spine head segments and assigning the neurite / glia type to
838 each process in three densely reconstructed (5 µm)^3 cubes of neuropil (same as in
839 previous section "ConnectEM classifier").

840 Together, these data were used to train one-versus-all TypeEM classifiers for axons,
841 dendrites, and astrocytes. The classifiers reached the following classification
842 performance on a separate test cube sized (5 µm)^3: Axon classifier: 91.8% precision
843 (P) and 92.9% recall (R); dendrite classifier: 95.3% P, 90.7% R; astrocyte classifier:
844 97.2% P, 85.9% R (at maximum area under precision-recall curve). The spine head
845 classifier was trained on a feature set calculated as above, with the exception that
846 the agglomeration step was omitted, and achieved 92.6% P and
847 94.4% R.

848 For subsequent processing, the TypeEM classifier scores were transformed to
849 probabilities using Platt scaling (Platt, 1999. Probabilistic Outputs for Support Vector
850 Machines and Comparisons to Regularized Likelihood Methods. In: Advances in

851 large margin classifiers.). Finally, the one-versus-all axon, dendrite, and astrocyte

852 probabilities of each segment were combined to multi-class probabilities by rescaling

853 them by the inverse of their sum.

Automated reconstruction of dendrites

855 For the reconstruction of dendrites, we first selected all SegEM segments with a

856 TypeEM dendrite probability (Fig. 1h) of at least 0.3 and a volume of at least 500 vx.

857 In the subgraph induced by these segments we deleted all edges that corresponded

858 to an interface of less than 300 vx size or a neurite continuity probability below 98%.

859 The graph was then used to cluster the dendritic segments into connected

860 components, yielding dendrite agglomerates.

861 To reduce the effect of TypeEM misclassifications, we used the fraction of

862 myelinated surface area to remove agglomerates from the dendrite class (calibrated

863 based on 50 random agglomerates with a myelinated surface fraction between 0.05

864 and 0.5): Agglomerates had a total volume of at least 200,000 voxels, had a

865 myelinated surface fraction above 0.25 (or above 0.08 if the agglomerate comprised

866 more than 25 segments); agglomerates did not contain somatic segments.

867 The myelinated surface fraction was calculated for each agglomerate with a total

868 volume of above 5 μm^3. All neighboring segments of the agglomerate were identified

869 according to the neighborhood graph, and the area of interfaces onto neighboring

870 myelin segments, defined as having at least 50% of their volume intersecting with

871 the myelin heuristic, were added up. This area was then divided by the total area of

872 all interfaces between the agglomerate and other segments.

Reconstruction of cell bodies (somata)

874 Cell bodies were reconstructed from the volume segmentation of each cell's nucleus

875 (see above). First, we identified all SegEM segments which were contained in a

876 nucleus with at least 50% of their volume. Then we added all direct neighbors of

877 these segments according to the neighborhood graph. Then we iteratively extended

878 the soma volumes along the neighborhood graph with the following constraints: only

879 consider segments with a size of at least 2,000 voxels and a center of mass at a

880 maximal distance of 8 μm from the center of mass of the corresponding nucleus;

881 only consider edges in the neighborhood graph with a continuity score above 0.98;

882 do not consider edges if the segments' vessel score or its myelin score were above
883 0.5. Then, all connected components of segments that were completely enclosed by
884 soma segments according to the neighborhood graph were added to the respective
885 soma. Finally, all segments with more than 80% of their surface adjacent to soma
886 segments were added iteratively (10 iterations).

Soma-seeded reconstruction of neurons

888 For the reconstruction of those neurons that had their cell body in the dataset (n=89
889 with dendrites reconstructed in the dataset, Fig. 1l,m, Suppl. Material 1), all dendrite
890 agglomerates from the automated dendrite reconstruction that overlapped with a
891 given soma volume (see previous section) were combined into one agglomerate for
892 each of the neurons.

Iterative semi-automated correction of whole cell agglomerates

894 The remaining errors in the soma-seeded neuron reconstructions (see previous
895 section) were corrected in a semi-automated procedure that consumed 9.7 hours for
896 all neurons, i.e. 5.18 minutes per neuron. Soma-based neuron reconstructions were
897 inspected for merger errors in the 3D view of webKnossos, and mergers were
898 corrected by deletion of nodes in the neighborhood graph of the neuron
899 reconstruction. Then, endings of the neuron were detected (see below), and
900 reconstructions at the endings were performed in webKnossos until a dendrite
901 agglomerate was reached that was obtained from the automated dendrite
902 reconstruction (see previous section). The inspection for mergers and the detection
903 of endings in the dataset was iterated until only real endings or endings at the
904 dataset boundary were left.

Automated axon reconstruction

906 For the reconstruction of axons, we first selected all SegEM segments with a volume
907 of at least 300 vx and a TypeEM axon probability (Fig. 1h) of at least 50%. The
908 subgraph induced by these segments was partitioned into connected components
909 (axon agglomerates) after removal of edges corresponding to interfaces with less
910 than 60 vx size or with a neurite continuity probability below 97%. Next, for each
911 segment that was part of an axon agglomerate, we computed the first principal
912 component of its voxel locations and used its degree of variance explanation as an

31

913 indicator for the directedness of the segment. We then determined for each interface

914 between the agglomerate's segments and all neighboring segments the alignment of

915 the interface's normal vector with the segment direction. Based on this, we obtained

916 an ending score for each interface of the segment, and at locations with high scores,

917 the axon agglomerate was grown into neighboring segments under the following

918 additional constraints: the neighboring segment had an axon probability of at least

919 30%; the interface had a size of at least 40 vx; the neighborhood graph edge had a

920 neurite continuity probability of at least 80%. This growth process was repeated ten

921 times.

922 Finally, we compensated for the heightened rate of merge errors in proximity to the

923 dataset boundary that results from decreased alignment quality. Edges that were

924 closer than 2 μm to dataset boundary and had a neurite continuity probability below

925 98% were removed from the axon agglomerates.

926 Then, all axon agglomerates of length 5 μm and above were used for the following

927 focused annotation steps. Length of agglomerates was computed as the summed

928 Euclidean length of all edges in the minimal spanning tree of the center of masses of

929 the agglomerate's segments.

FocusEM ending detection and query generation

931 To determine the endings of axons at which focused annotation could be seeded, we

932 used the following procedure. For each segment in an axon agglomerate we took the

933 segments that are direct graph neighbors or that come within 1 μm distance, and

934 computed the first principal component of their volume. We then identified all

935 segments where the principal component of the local surround explains at least 50%

936 of the variance, and determined the borders on the axon agglomerate surface that

937 were aligned to that axis (i.e., all interfaces for which the vectors from the center of

938 mass of the local surround to the center of mass of the interface were at an angle of

939 at most $\cos^{-1}(0.8) \approx 37$ °). Finally, the identified interfaces were grouped using a

940 cutoff distance of 600 nm and reduced to the interface best aligned to the surround's

941 principal component. We determined the point within 500 nm of each interface that is

942 closest to the core of the axon agglomerate and used it together with the principal

943 component of the local surround as the start position and orientation of a focused

32

944 annotation query in webKnossos. Interfaces within 3 µm of the dataset boundary
945 were excluded from query generation.

946 FocusEM axon queries were performed in webKnossos flight mode. The volume
947 map of all axon agglomerates larger than 5 µm was used to dynamically terminate
948 flight paths when a user entered already reconstructed agglomerates (this was
949 implemented in a custom script using the webKnossos frontend APITo reduce the
950 delay between subsequent queries, we implemented a "hot switching mode" in
951 webKnossos such that the next query was already loaded in the background while
952 answering the current query. With this, an immediate switching (amounting to a
953 jumping to query locations in the dataset) was possible that yielded negligible lag
954 between tasks.

955 **Query analysis**

956 FocusEM queries yielded linear skeletons from webKnossos flight mode. For each
957 node of a given skeleton we determined the overlap with axon agglomerates in the
958 $(3 \text{ vx})^3$ cube around each skeleton node (a skeleton was considered to overlap with
959 an axon agglomerate if the agglomerate was contained in at least 54 vx around the
960 skeleton nodes). For the overlapping agglomerates, we determined the
961 corresponding agglomerate endings within 300 nm distance from the skeleton
962 nodes. Based on the configuration of agglomerate overlaps, agglomerate endings
963 reached by the queries and proximity of the query to the dataset boundary, the query
964 results were either accepted as is, re-queried or discarded (see code files below for
965 detailed decision tree). When locations were queried multiple times, the information
966 on agglomerate and ending overlap was used to keep only minimal subsets of
967 skeleton tracings for the final axon agglomerates (see "Iteration between ending and
968 chiasma detection"). For connectome analysis and display, volume segments that
969 had not yet been assigned to any axon agglomerate and that overlapped with the
970 user skeleton from the flight mode queries were collected and added to the
971 agglomerate volume.

972 **Chiasma detection and queries**

973 To identify mergers, we detected geometric configurations (Fig. 1k) with more than
974 two-fold neurite crossings after agglomeration. Chiasmata were detected by counting

33

the number of intersections of the graph representation of a given agglomerate with a sphere centered on the nodes of the graph. For this, the agglomerate was reduced to the connected component contained within a sphere of 10 µm radius around the current node, and then all edges within a sphere of radius of 1 µm were removed. The remaining graph components were considered sphere exits. If four or more sphere exits were found, the node at the sphere center was labeled as a chiasmatic node. Within axon agglomerates, the chiasmatic nodes were clustered using a cutoff distance of 2 µm and subsequently reduced to the node closest to the center of mass of the cluster. At these locations, queries from the sphere exits pointing towards the sphere center were generated and annotated as described for the ending queries (Fig. 1n,o). The webKnossos flight mode annotations of chiasma queries were stopped when the annotator left the bounding box around all exit locations.

Chiasma query interpretation

To decide which of the exits contributing to a given chiasma should remain connected and which should be disconnected, we used the query results from all chiasma exits. The full set of results enabled the detection of chiasmata with contradictory query answers, partial automated error correction, and the re-querying of a minimal set of exits. Chiasmata with a full and contradiction-free set of answers were solved by removing the edges within the center 1µm sphere from the agglomerate mst and by subsequent reconnection of the exits based on a minimal set of flight queries.

Iteration between ending and chiasma detection

Following automated axon reconstruction, the FocusEM queries for ending and chiasma annotations were applied iteratively.

Spine head agglomeration

Spine heads were agglomerated by connecting neighboring segments with a TypeEM spine head probability above 50% that were connected by an edge with neurite continuity probability of at least 98%. Spine head detections within blood vessels were discarded. This yielded 415,797 spine head agglomerates.

Spine attachment

Of the 415,797 spine head agglomerates, 5.6% got attached to a dendritic shaft during automated dendrite agglomeration (see above). We then implemented a greedy walk strategy from spine heads to the corresponding dendritic shafts. The walk was terminated upon reaching a dendrite agglomerate of at least ~1.1 µm^3 ($10^{5.5}$ vx) and was restricted to at most ten steps along continuity edges, each having a neurite continuity probability of 25% or more and only involving segments with axon probability below 80%. With this, an additional 206,546 (49.7%) spine heads could be attached to the corresponding dendrite. For the remaining spines, SegEM mergers in the very thin spin necks typically prevented the spine attachment heuristics to be successful. We instead seeded manual annotation in the 164'969 remaining spine heads with a distance of at least 3 µm from the dataset boundary, asking annotators to connect these to the dendritic shafts. This consumed 900 work hours total and resulted in a final spine head recall of 88.6% for spine heads further than 10 µm from the dataset boundary.

Synapse agglomeration

Synaptic interface candidates (n = 864,405 out of which 605,569 were onto spine segments and 258,836 onto other segments) detected by interface classification were discarded if the score both synapse scores were larger than -2 or the continuity probability of the corresponding edge was larger than 0.7, or the myelin score of the pre- or postsynaptic segment was larger than 0.375 or the presynaptic segment was contained in the soma volumes. The remaining synaptic interface candidates (n= 862,350) were restricted to those with a center of mass more than 3 µm from the segmentation volume boundary (yielding n=696,149 synaptic interfaces with a pre- and postsynaptic segmentation object, each, that are used in the following analyses).

To consolidate synaptic interfaces, the following steps were applied: First, all presynaptic segmentation objects contributing to any of the synaptic interfaces were combined, if they were connected to each other by at most two steps on the segmentation neighborhood graph with each step along an edge above 0.98 ConnectEM score. The same was applied to all postsynaptic segmentation objects. Then, all synaptic interfaces between the combined pre – and postsynaptic segmentation objects were combined into one synapse, each. Synapse

35

agglomerates for which at least one postsynaptic segment was part of the spine head agglomerates were considered as spine synapse agglomerates. A spine synapse agglomerate was called "primary spine innervation" if it contained the interface with the highest SynEM score onto a given spine head agglomerate, and "secondary spine innervation" otherwise. Multiple synapse agglomerates between an axon agglomerate and a spine head agglomerate were merged into a single synapse agglomerate. The center of mass for a synapse agglomerate was calculated as the component-wise mean of the centers of mass of the individual interfaces. The area of a synapse agglomerate was calculated as sum of the border areas of the individual interfaces.

Soma synapse exclusion heuristic

Synapse agglomerates for which at least one postsynaptic segment was part of the soma agglomerates were considered as soma synapses. Synapse agglomerates were clustered based on their center of mass using hierarchical clustering with single linkage and a distance cutoff of 1 µm. If a synapse agglomerate cluster contained a spine synapse which was the only synapse onto the corresponding spine head agglomerate, then all soma synapses of the synapse agglomerate cluster were discarded. Synapses from excitatory axons onto somata of spiny cells were ignored for the analysis of subcellular target specificity and geometric predictability.

Connectome aggregation

The connectome was constructed using the axon agglomerates, postsynaptic agglomerates (dendrites, somata and axon initial segments), and synapse agglomerates. For each pair of an axon and postsynaptic agglomerate, all synapse agglomerates that had a presynaptic segment in the axon agglomerate and a postsynaptic segment in the postsynaptic agglomerate were extracted and associated with the corresponding axon-target connection. The total number of synapses of a connection was defined as the number of synapse agglomerates associated with that connection. The total border area of a connection was defined as the sum of the border area of all synapse agglomerates. All of the following analyses were restricted to axons with at least ten output synapses.

Target Class Detection Heuristics

36

1068   To determine the post-synaptic target classes apical dendrites (AD), smooth
1069   dendrites (interneuron dendrites, SD), axon initial segments (AIS), proximal
1070   dendrites (PD) and cell bodies (SOM), the following heuristics were used:

1071   Cell bodies were identified based on the detection of nuclei as described in
1072   "Reconstruction of cell bodies". The non-somatic postsynaptic components of the
1073   soma-based neuron reconstructions were marked as proximal dendrites. Smooth
1074   dendrites were identified by having a spine rate (i.e., number of spines per dendritic
1075   trunk path length) below 0.4 per μm (Kawaguchi, Karuba, Kubota, 2006), Fig. 2d,
1076   unless identified as apical dendrites. For the analysis of target class specificities and
1077   geometric predictability, the dendrites of soma-based interneuron reconstructions
1078   were considered as smooth, but not proximal dendrites.

1079   For the identification of apical dendrites, all dendrite agglomerates that intersected
1080   with the pia- and white matter-oriented faces of the dataset were manually inspected
1081   in webKnossos (total of 422 candidates, total inspection time 5 hours for an expert
1082   annotator) with the inspection criteria: directed trajectory along the cortical axis;
1083   maximally two oblique dendrites leaving the main dendrite; spine rate of non-stubby
1084   spines of at least about one every two micrometers.

1085   Contradictory class assignments between SD and AD occurred for 46 dendrites and
1086   were resolved by manual inspection in webKnossos.

1087   The axonal part of soma-based neuron reconstructions which was more proximal
1088   than the first branch point was considered as axon initial segment. Vertically oriented
1089   agglomerates that entered the dataset from the pia-end of the dataset and had no
1090   spines or output synapses, and transitioned into a clearly axonal process closer to
1091   the white matter boundary of the dataset were also identified as axon initial
1092   segments.

1093

1094   Definition of inhibitory and excitatory axons

1095   Inhibitory and excitatory axons were separated based on the fraction of their
1096   synapses marked as primary spine innervations (see "synapse agglomeration") (Fig.
1097   3a). To automatically resolve remaining merge errors between these two axon

37

1098 classes, we split axons between the two modes of the spine rate distribution (20 to

1099 50% of synapses being primary spine innervations) at all their branch points (see

1100 "Chiasma detection and queries"). Then, we defined excitatory axons as those with

1101 more than 50% of synapses being primary spine innervations and termed axons with

1102 less than 20% primary spine innervations inhibitory.

Definition of thalamocortical axons

1104 To identify those excitatory axons that were likely originating from the thalamus we

1105 used the fact that thalamic axons from VPM have been described to establish large

1106 multi-synaptic boutons at high frequency in mouse S1 cortex ((Bopp et al., 2017);

1107 see Fig. 3h,i). We quantitatively applied these criteria by measuring the density of

1108 primary spine innervations (PSI) per axonal path length, the average number of PSI

1109 per axonal bouton, the fraction of axonal boutons with multiple PSIs, and the median

1110 bouton volume. Boutons were defined as clusters of PSI with an axonal path length

1111 of less than 2.4 μm between the cluster centers. In a calibration set of ten manually

1112 identified corticocortical and ten thalamocortical axons these features were

1113 discriminatory. We combined them into a single thalamocortical axon probability

1114 using logistic regression. Excitatory axons with a TC probability of at least 60% were

1115 identified as thalamocortical.

Subcellular specificity analysis

1117 First, we assumed that all synapses of a given axon class have the same probability

1118 to innervate a particular postsynaptic target class (as above). We then inferred this

1119 first-order innervation rate for each axon- and postsynaptic target-class by searching

1120 for the probability which best explains whether or not an axon innervated the target

1121 class under a binomial model. The optimized binomial model was then used together

1122 with the measured number of synapses of each axon to calculate the expected

1123 distribution of target innervation rates. A one-sided Kolmogorov-Smirnov was used to

1124 test for the existence of a subpopulation with increased target innervation rate. To

1125 identify those axons that innervated a given target class beyond chance (Fig. 3k), we

1126 computed the probability $p^{(t)}_{meas,i,k}$ of finding at least the measured fraction of

1127 synapses onto target t for each axon i from axon class k. The p-values were also

1128 calculated for the expected distribution of target innervation rates and combined with

38

1129 $p^{(t)}_{meas,i,k}$ to estimate the p-value threshold $\hat{p}^{(t)}_k$ at which the false discovery rate q

1130 (Storey and Tibshirani, 2003) crosses 20%. 80% of the axons with $p^{(t)}_{meas,i,k} < \hat{p}^{(t)}_k$

1131 are innervating target t with a rate above the first-order innervation probability and

1132 are thus called to be t-specific.

1133 For the analysis of 2nd order innervation specificity (Fig. 3l,m), we reported the

1134 fraction of synapses onto target τ by t-specific axons of class k after removal of

1135 synapses onto t. This innervation rate was compared against the fraction of

1136 synapses onto target τ by all axons of class k.

Geometrical predictability analysis

1138 To determine whether the found innervations can be predicted by geometrical

1139 measurements we used the following model: For each axon we determined the total

1140 surface area of the target classes that were contained within the cylinder of radius

1141 r_{pred} around the axon (Fig. 4a-c) and compared it to the actually innervated target

1142 fraction of each axon (Fig. 4c,d). We then analyzed the correlation between the

1143 availability of the target surfaces and the actually established synapses on these

1144 target classes (Fig. 4e).

1145 To obtain an overall predictability quantification, we then computed the coefficient of

1146 determination (R^2) using the following model: For all axons of given type, we used

1147 the fraction of target innervations and fractional surface availabilities in a given

1148 surround of radius r_{pred} to find the optimal multivariate linear regression parameters.

1149 To estimate best-case geometric predictability, we then calculated the R^2 value as 1

1150 minus the ratio of the residuals to synaptic variance on the same axons used for

1151 parameter optimization, while correcting for the variance introduced by the finite

1152 number of synapses per axon. Accordingly, we used the axons' fractional surface

1153 availabilities within r_{pred} and absolute synapse numbers to calculate the expected

1154 binomial variance, and subtracted it from the squared residuals. If the remaining

1155 squared residual of an axon was negative after correction, it was set to zero.

1156 This analysis made several assumptions that were in favor of a geometrical

1157 explanation of synaptic innervation (therefore the conclusions about a minimal

predictability (Fig. 4f) are still upper bound estimates): it was assumed that the number of synapses for a given axon was already known; in most settings, only average synapse rates are known for a given circuit; it also assumed that a precise knowledge of the axonal trajectory and the surrounding target surface fractions were available; again, this is usually only available as an average on the scale of r_{pred} of several 10's of micrometers.

To relax the assumption of complete knowledge about target availabilities, we repeated the above R^2 analysis for a model in which the predicted fractional innervation of a target is the fractional surface availability of that target.

Synaptic input / output maps and spatial synapse distributions

To determine the spatial distribution of synaptic inputs along dendrites, we used the soma-based neuron reconstructions and determined for each synapses onto their dendrites the shortest pairwise path length between all somatic and postsynaptic segments (Fig. 5a,b). Input synapses were assigned the class of the corresponding axon (as described above) and then pooled over all neurons. Synapses originating from axons of unknown type (e.g., axon had less than ten synapses and thus was excluded from classification) were ignored. The spatial output map was derived from axon tracings, which were seeded in all somata and then mapped onto the segmentation (see "Query analysis") to find output synapses based on segment overlap (Fig. 5c,d).

The spatial synapse distribution of a given axon class was obtained by projecting the center of mass of the corresponding synapses (see "Synapse agglomeration") onto the XY plane, where X is the pia-white matter axis, and then calculating a kernel density estimate thereof (Fig. 5e). The synapse ratio along the cortical axis was computed as the ratio of absolute synapse counts per histogram bin (Fig. 5f-h).

To quantify the effect of soma location on synaptic innervation, we calculated for each soma-based neuron reconstruction the center of mass of all somatic segments, and the fraction of excitatory input synapses that originate from thalamocortical axons. We performed multivariate linear regression in the YZ plane orthogonal to the cortical axis and corrected the measured synapse fraction before quantifying the effect of cortical depth using univariate linear regression.

1189   Finally, the soma-based neuron reconstructions were manually split into their primary

1190   dendrites to assess the effect of dendritic orientation on synaptic inputs. The

1191   orientation of a dendrite was calculated as the volume-weighted mean of the unit

1192   vectors from the soma (as above) to the center of mass of the corresponding SegEM

1193   segments. Finally, the dot product *dp* of the resulting vector (after renormalization)

1194   with the unit vector along the cortical axis was put in relation to the ratio of the

1195   dendritic synapse fraction to the synapse fraction of the corresponding neuron. The

1196   linear regression of these two quantities was evaluated based on the coefficient of

1197   determination, whereas the pia- (*dp* < -0.5) and white matter-oriented dendrites (*dp* >

1198   0.5) were compared based on a two-sample *t*-test.

Synapse-size consistency analysis

1200   To determine the consistency of primary spine synapses between a given axon-

1201   dendrite pair, we calculated the axon-spine interface area (ASI, (de Vivo et al., 2017)

1202   (Staffler et al., 2017)) of a synapse as the total contact area between the

1203   corresponding axon and spine head agglomerates. For axon-dendrite pairs

1204   connected by exactly two primary spine synapses, we then calculated the coefficient

1205   of variation (CV) of the ASI areas by $CV = 2^{1/2} (ASI_1 - ASI_2) / (ASI_1 + ASI_2)$ with ASI_1

1206   and ASI_2 being the larger and smaller of the two ASI areas, respectively. To avoid

1207   false same-axon same-dendrite (AADD) pairs caused by remaining merge errors in

1208   the axon reconstruction, this analysis was performed only after splitting all axons at

1209   all branch points. The measured distribution of CV values was compared against the

1210   CV values obtained by randomly drawing pairs from the observed ASI area

1211   distribution (Fig. 6e,f). To test whether same-axon same-dendrite (AADD) primary

1212   spine synapse pairs have a lower CV than random pairs, a one-sided Kolmogorov-

1213   Smirnov test was used. The critical CV value that defines the upper limit of the range

1214   in which AADD pairs occur more often than expected was determined by searching

1215   for the intersection of the kernel density estimates of the observed and expected CV

1216   distributions. A lower bound on the fraction of overly-consistent primary spine

1217   synapse pairs is given by the difference between the cumulative probability functions

1218   of the two distributions at the critical CV value. Finally, we built kernel density

1219   estimates of the probability density function over the two-dimensional space defined

1220   by the CV and mean $\log_{10}(ASI)$ for AADD pairs, random pairs, and random pairs of

1221   AADD synapses. The differences between these density estimates were used to

41

1222   extract the non-random components in CV-ASI relationship of AADD pairs relative to

1223   random pairs and random pairs of AADD synapses, respectively.

Comparison between dense reconstructions

1225   For the comparison of published dense reconstructions and the invested resources

1226   (Fig. 1p,q), we used the following numbers: Dense reconstruction in the mouse

1227   retina (Helmstaedter et al., 2013): about 640 mm reconstructed neuronal path length,

1228   about 20,000 invested work hours; Dense reconstruction in the mouse cerebral

1229   cortex (Kasthuri et al., 2015): 6.75 mm of path length reconstructed within 253 hours

1230   (37.5 h/mm, 4.5 μm/μm^3, 1500 μm^3 reconstructed; see (Berning et al., 2015) for

1231   derivation of numbers); Dense reconstruction in the zebrafish olfactory bulb (Wanner

1232   et al., 2016b): 492 mm path length with 25,478 invested work hours; Dense

1233   reconstruction in the fly larval nervous system (Eichler et al., 2017): 2.07 meters

1234   (based on skeleton reconstructions in Supplement of (Eichler et al., 2017)) with

1235   28,400 hours investment (73 μm / h; see (Schneider-Mizell et al., 2016)); L4 dense

1236   reconstruction: 2.724 meters (of these in mm: dendritic shafts 342, dendritic spines

1237   551, dendrites connected to a cell body in the volume 62.5, axons connected to a

1238   cell body in the volume 6.5; axons 1760; note about 80% of the volume is dense

1239   neuropil) within 3,982 hours.

1240

Computational cost estimate

1242   For the estimation of the total computational cost, a runtime of 5 hours for SynEM,

1243   72 hours for TypeEM and 24 hours for all other routines on a cluster with 24 nodes

1244   each with 16 CPU cores and 16 GB RAM per core was used. The runtime was

1245   converted to resources using 0.105 USD/h per CPU core with 16 GB RAM (Amazon

1246   EC2: 6.7 USD/h for 64 CPU cores with 1000 GB RAM). The computational cost for

1247   Flood-Filling Networks was calculated using 1000 GPUs that ran for a total wall time

1248   of 16.02 hours (Suppl. Table 3, (Januszewski et al., 2018)) and a cost of 0.9 USD/h

1249   for a single GPU which was multiplied by the ratio of the sizes of our dataset (61 x 94

1250   x 92 μm^3) and the dataset used in (Januszewski et al., 2018) (96 x 98 x 114 μm^3).

1251

Error Measurements

To quantify the errors remaining after axon reconstruction, we chose the same 10 randomly selected axons (total path length, 1.72 mm) that had also been used for error rate quantification in (Boergens et al., 2017). These axons were not part of any training or validation set in the development of FocusEM. Repeating the analysis described in (Boergens et al., 2017) for the largest axon agglomerate overlapping with the ground truth axon, respectively, yielded a total number of 22 errors, of which 15 were continuity errors (compare to panels 1l,m in (Boergens et al., 2017)).

The error rates and recall of soma-based dendrite reconstructions were calculated from proofread ground truth annotations comprising a total of 89 cells and 64.08 mm path length. Each node of the ground truth skeleton was marked as recalled if it overlapped with the corresponding dendrite agglomerate (see "Query analysis"), or flagged invalid if placed outside the segmented volume. A ground truth edge was considered recalled if both end nodes were recalled, or invalid if any of the end nodes was invalid. 54.51 mm, or 87.3%, of the 62.46 mm valid ground truth path length were recalled. Split errors, by definition, result in partial dendrite reconstructions and were thus detected as non-recalled ground truth fragments with at least 5 µm path length. The detected were proofread, yielding a total of 37 split errors.

The identification of axonal target specificity (Fig. 3) was insensitive to split- and merger errors, because as long as axonal reconstructions were long enough to provide meaningful statistical power for the analyses, split axons were expected to correctly sample target specificities and mergers of axons were expected to only dilute specificities. Therefore the results about the existence of target specific inhibitory and excitatory axon classes represent a lower bound of specific wiring. The results on the lack of geometric predictability (Fig. 4) were similarly unaffected by remaining split and merge errors.

For the finding that no inhibitory axons show target specificity for AIS in L4 (Fig. 3i), however, we needed to control that this lack of specificity was not induced by remaining axonal merge errors. We manually inspected a subset of 10 axons innervating AIS. Only one synapse (out of more than 100 synapses) was erroneously

43

1283 added to an AIS innervating axon due to a merger, thus providing no evidence that
1284 the lack of AIS target specificity could be an artifact of merged axons.

1285 For the results on synaptic input composition (Fig. 5) we varied the sensitivity of our
1286 detection of TC axons and found that also for detections with a higher TC axon recall
1287 and a lower recall at higher precision the conclusions were unchanged.

1288 The results on synaptic size consistency could be strongly affected by the remaining
1289 merge errors in axons, diluting data on consistent synapses when merging unrelated
1290 axons together. To control for this, we obtained the results in Fig. 6 using axons for
1291 which all 3-fold intersections in all axons had been artificially split before the
1292 analysis. For the results in Fig. 3, we repeated analyses after splitting of axons and
1293 found the key conclusions unaltered.

1294

Statistical methods

1295

1296 The following statistical tests were performed (in order of presentation in the figures):

1297 The existence of axon subpopulation with unexpectedly high synapse rate onto a
1298 given target class was tested using the one-sided Kolmogorov-Smirnov test (Fig.
1299 3i,j). Axons belonging to a given target-specificity class were identified based on the
1300 false detection rate criterion (q=20%, (Storey and Tibshirani, 2003)) (Fig. 3k).

1301 The degree to which synaptic variance is explainable by geometry-based models
1302 was evaluated using the coefficient of determination (R^2) (Fig. 4f). Binomial variance
1303 was corrected for by subtracting the surface fraction-based expected binomial
1304 variance from the squared residuals. The result was set to zero, if negative.

1305 Path-length dependent axonal synapse sorting was tested using a two-sided t-test.
1306 F-tests were used to evaluate synaptic gradients as function of cortical depth (Fig.
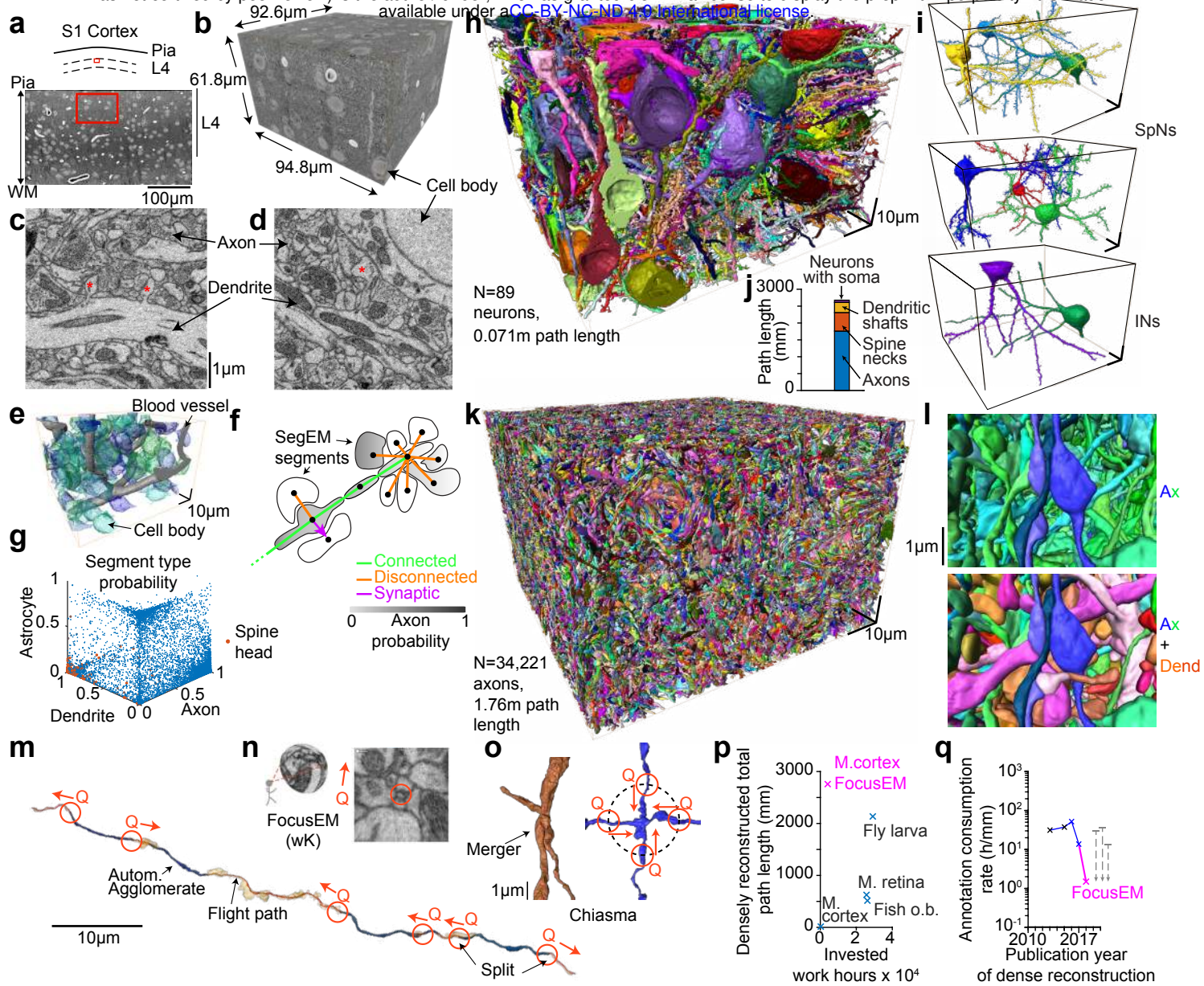1307 5f,h) or dendritic orientation (Fig. 5j).

1308 To test whether the axon-spine interface areas of a given spine synapse pair
1309 configuration were more similar than randomly sampled pairs, a one-sided
1310 Kolmogorov-Smirnov test was used (Fig. 6e).

Data availability, software availability

1311

44

1312   All raw segmentation data, skeleton annotations, connectomic data, and software

1313   developed and used in this study will be made publicly available upon publication.

1314

1315

a S1 Cortex
Pia
L4
Pia
WM
100µm

b 92.6µm
61.8µm
L4
94.8µm
Cell body

c Axon
Dendrite
1µm

d Cell body

e Blood vessel
Cell body
10µm

f SegEM segments
Connected
Disconnected
Synaptic
Spine head
Axon probability

g Segment type probability
Astrocyte
Spine head
Dendrite
Axon

h N=89 neurons, 0.071m path length

i SpNs
INs

j Neurons with soma
Path length (mm)
Dendritic shafts
Spine necks
Axons

k N=34,221 axons, 1.76m path length

l Ax
Ax + Dend
1µm

m Q
Q
Autom. Agglomerate
Flight path
Split
10µm
Q
Q
Q
Q

n FocusEM (wK)
Q

o Merger
Chiasma
1µm
Q
Q
Q

p M.cortex
FocusEM
Fly larva
M. retina
M. cortex
Fish o.b.
Densely reconstructed total path length (mm)
Invested work hours x 10⁴

q Annotation consumption rate (h/mm)
FocusEM
Publication year of dense reconstruction

2018 L4 dense
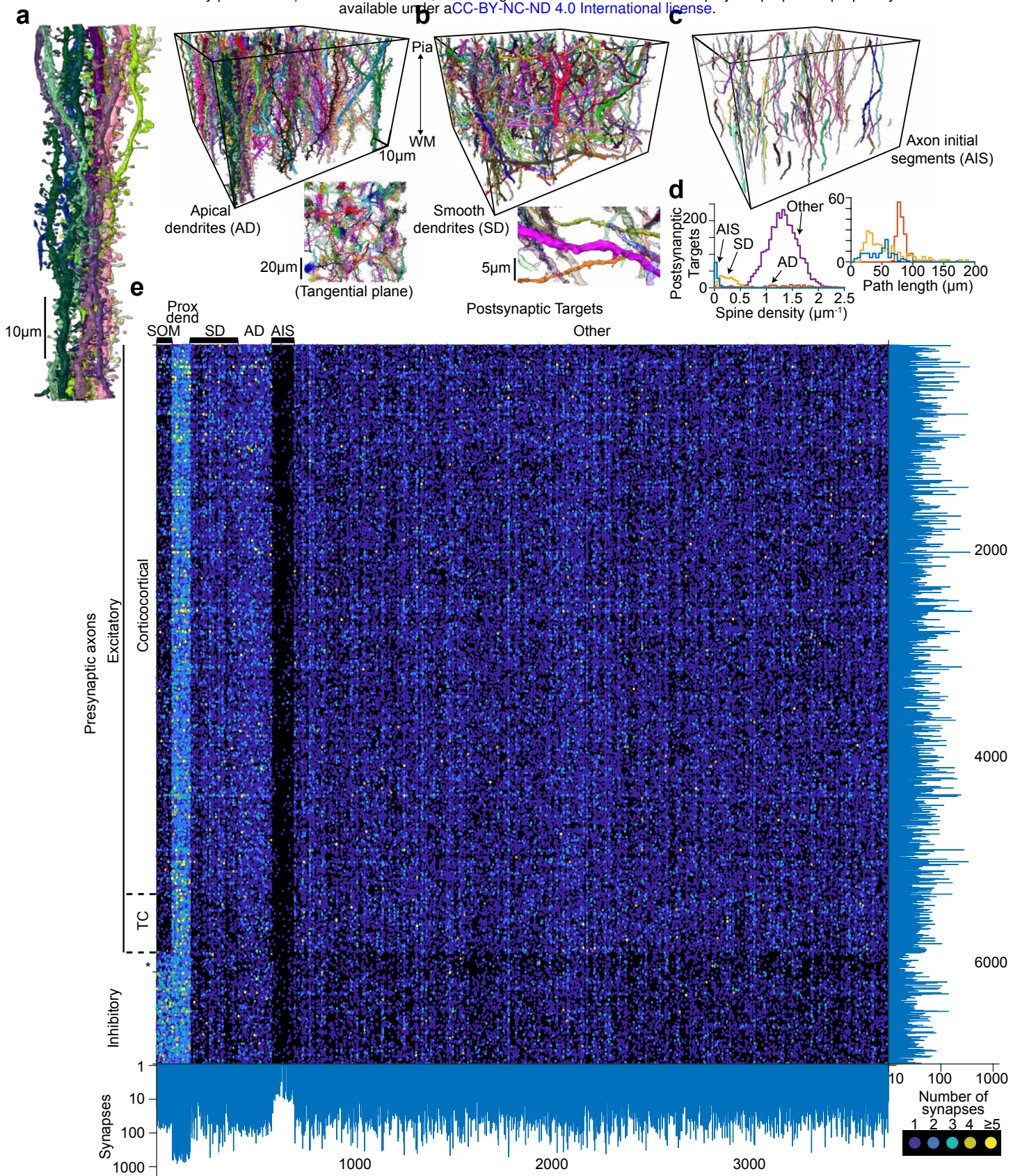**Figure 1**

1316   **FIGURE LEGENDS**

1317

1318   **Figure 1**

1319   **Dense connectomic reconstruction of cortical neuropil from layer 4 of mouse**

1320   **primary somatosensory cortex.** (a-d) Location (a, red) of 3D EM dataset (b), WM:

1321   white matter; high-resolution example images (c,d). Asterisk, examples of dendritic

1322   spines. (e) Low-resolution automated reconstruction of cell bodies (blue-green) and

1323   blood vessels (gray). (f) Sketch of FocusEM, a set of methods for semi-automated

1324   reconstruction of dense EM data. Sketch illustrates neurite segments obtained from

1325   SegEM (Berning et al., 2015), their neighborhood graph (dots and lines), the

1326   classification results for connected neurite pieces and synaptic interfaces, and a cell

1327   type classifier used to determine the neurite and/or glia type. For details see

1328   Methods. (g) Classification result of the neurite/glia type classifiers; red: spine head

1329   segments. (h) Reconstruction of all neurons with a cell body and dendrites in the

1330   dataset (n=89, total path length of 0.069 m, thus only 2.6% of the path length in the

1331   tissue volume, see j). (i) 6 spiny example neurons (SpNs, top, middle) and 2

1332   interneurons (INs, bottom); see Supplementary Material 1 for gallery of all neurons.

1333   (j) Quantification of circuit components in the dense reconstruction. Note the majority

1334   of circuit path length (total: 2.68 m) is contributed by non-proximal axons (1.78 m,

1335   66.4%), spine necks (0.55 m, 20.5%), and dendritic shafts (0.28 m, 10.4%) not

1336   connected to any cell body in the volume. (k) Display of all reconstructed 34,221

1337   axons contained in the dataset. (l) Zoom into the dataset illustrating density of axons

1338   (Ax, top, blue-green) and comparison to effective prevalence of dendrites (Dend,

1339   bottom, orange-red) at an example location. (m-o) Focused annotation strategy

1340   (FocusEM) for directing human annotation queries (Q, red) to ending locations of the

1341   automatically reconstructed axon pieces (m, blue). Human annotators were oriented

1342   along the axon's main axis to trace its continuity in webKnossos using flight mode (n,

1343   (Boergens et al., 2017)) yielding flight paths of 5.5 ± 8.8 μm length (21.3 ± 36.1 s per

1344   annotation, n= 242,271). To detect and correct neurite mergers after automated

1345   outgrowth of neurites, locations of chiasmatic shape (o) were detected, and queries

1346   (Q) directed from the exits of the chiasma towards its center to determine correct

1347   continuities (see Methods). (p,q) Quantification of circuit size and invested work

46

1348 hours for dense circuit reconstructions so far performed in connectomics, and

1349 resulting order-of-magnitude improvement provided by FocusEM compared to

1350 previous dense reconstructions (q). Fish o.b.: Zebrafish olfactory bulb (Wanner et al.,

1351 2016a; Wanner et al., 2016b); M. retina: Mouse retina IPL (Helmstaedter et al.,

1352 2013); Fly larva: mushroom body in larval stage of D. melanogaster (Eichler et al.,

1353 2017); M. cortex: (Kasthuri et al., 2015) and this study (magenta). Note that only

1354 completed dense reconstructions were included in the comparison. Scale bars in c

1355 apply to d; h apply to i.

1356

2018 L4 dense

Figure 2

1357 **Figure 2**

1358 **Postsynaptic target classes and dense cortical connectome. (a-d)** Display of all

1359 apical dendrites (AD, a, magnified one apical dendrite bundle (left), and top view in

1360 tangential plane illustrating AD bundles), smooth dendrites (SD, b, magnification

1361 inset illustrates low rate of spines), axon initial segments (AIS, c) and their respective

1362 path length and spine density distributions (d). **(e)** Display of connectome between

1363 all axons (n=6,979) and postsynaptic targets (n=3,719) in the volume with at least 10

1364 synapses, each; total of 153,171 synapses (of 388,554 synapses detected in the

1365 volume). Definition of postsynaptic target classes, see (a-d); definition of presynaptic

1366 axon classes: see Fig. 3. Note that for AIS also those with less than 10 input

1367 synapses are shown. SOM: neuronal somata; Prox. Dend.: proximal dendrites

1368 connected to a soma in the dataset; asterisk, remaining unassigned axons (see Fig.

1369 2b).

1370

1371

48
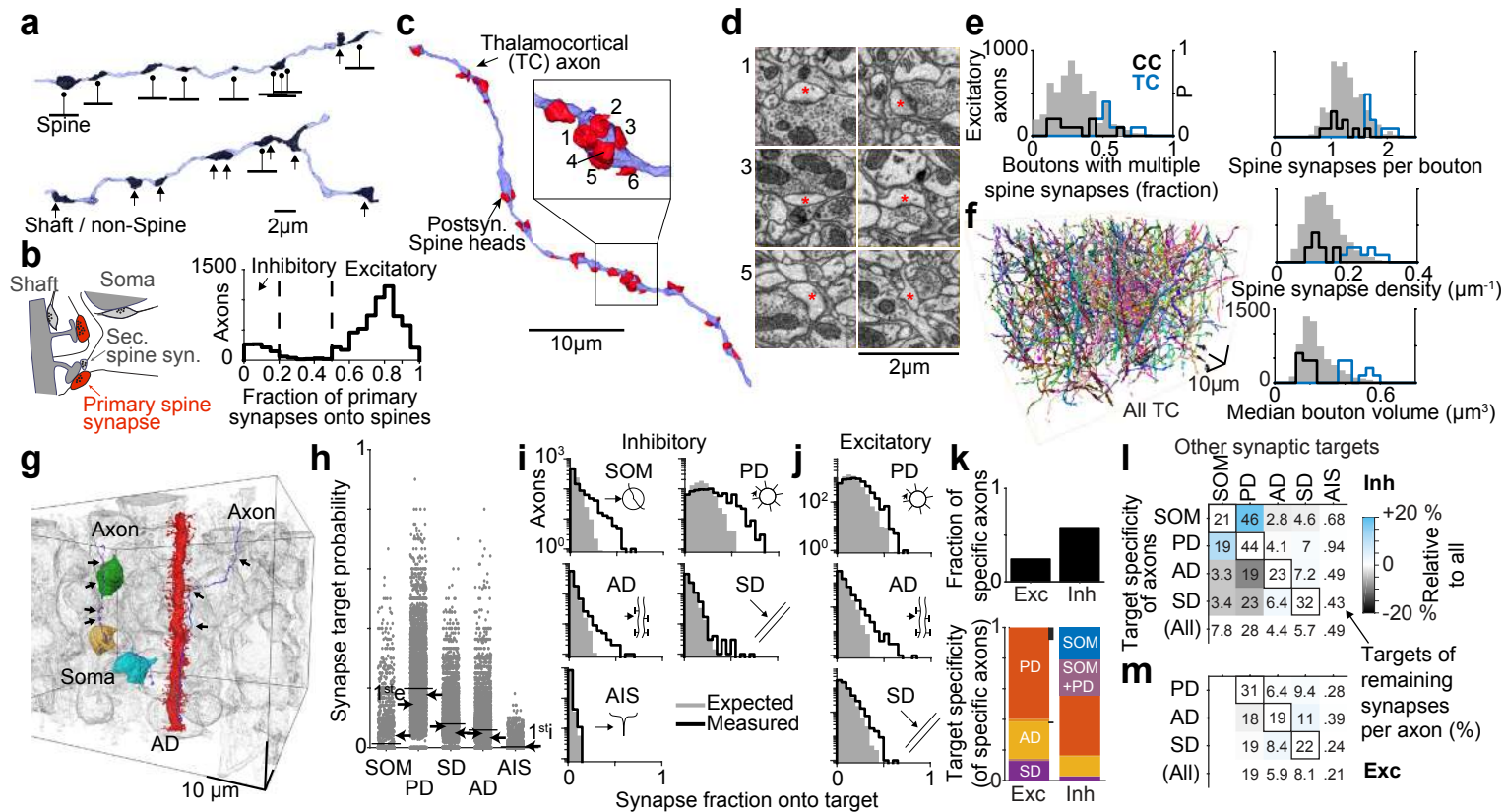
2018 L4 dense

Figure 3

Figure 3

Connectomic definition of axon classes. (a) Example axons with high (top) and low (bottom) fraction of output synapses made onto dendritic spines. (b) Distribution of spine targeting fraction over all n=6,979 axons; dashed lines indicates thresholds applied to distinguish non-spine preferring, likely inhibitory (i, <20% spine innervation, n=893, 12.8% of all axons) from spine-preferring, mostly excitatory (e, >50% spine innervation, n=5,894, 84.5% of axons) axons. Sketch illustrates measurement of spine fraction as fraction of primary spine innervations out of all other synapses. (c-e) Identification of thalamocortical axons by previously established criteria (Bopp et al., 2017) relating to their high frequency of multiple-target large boutons (example in c,d; red asterisks, postsynaptic spine heads of same TC bouton). Quantification of these properties for all excitatory axons (gray shaded) and test sets of clear thalamocortical (TC, blue) and cortico-cortical (CC, black) axons (relative distributions, right axes). (f) Resulting set of n=569 TC axons in dataset. (g-m) Connectomic evidence for subcellular target specificity of certain axon classes. (g) Two example axons innervating three somata (SOM, left, n=8 synapses onto somata of 18 total) and an apical dendrite (AD, right, n=2 synapses onto AD of 13 total), respectively. All other cell bodies and ADs in gray. (h) Overall fraction of synapses onto SOM, PDs, ADs, SDs, AIS for all n=6,979 axons. Arrows indicate binomial probabilities over axons to establish at least one synapse onto the respective target (1^{st}e for excitatory axons, arrow pointing right; 1^{st}i for inhibitory axons, arrows pointing left). Black lines, average over axons. (i) Comparison of predicted synapse fraction onto target classes per inhibitory axon based on the binomial probability (p_{1sti}, see h) to innervate the target at least once (gray shaded) and measured distribution of synapse fractions onto targets (black lines). Note longer tail of measured innervation fraction in measured *vs.* expected data for SOM, PD, AD and SD, but not AIS. (j) Same analysis as in (i) for excitatory axons indicates AD-, PD- and SD-specificity. (k) Fraction of target-specific excitatory (Exc) and inhibitory (Inh) axons identified using the false detection rate criterion (q=20%, (Storey and Tibshirani, 2003)). Black bars indicate TC axons. Mixed colors indicate axons specific for both SOM and PD. (l,m) 2nd order innervation pattern for target-specific axons; numbers report fractional innervation by non-class specific, remaining synapses per axon; colors indicate under- (blue) or over-(red)-frequent innervation.

49

1405   Diagonal entries report fraction of synapses onto same specific target (black boxes).

1406   The conditional dependence of target innervation especially for the inhibitory axon

1407   classes in this 2nd order analysis serves as *post-hoc* evidence of the connectomic

1408   definition of axonal types as shown in (a-k).

1409
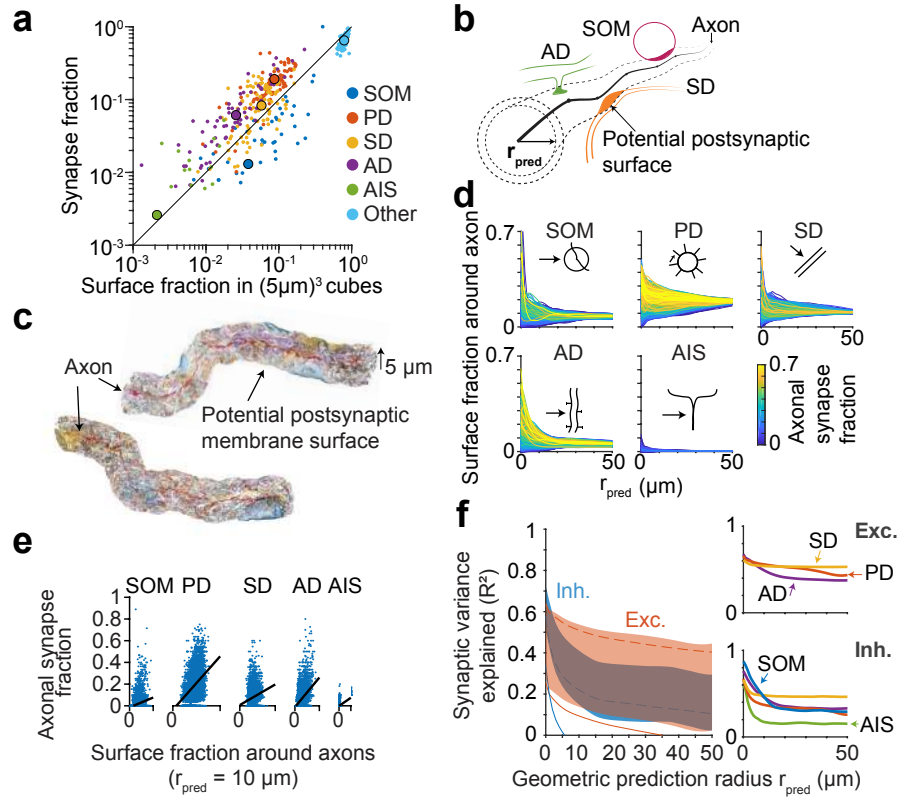
2018 L4 dense
Figure 4

1410 **Figure 4**

1411 **Contribution of neurite geometry and postsynaptic membrane availability to**

1412 **cortical wiring. (a)** Comparison between the fraction of membrane surface area

1413 attributed to one of the subcellular target classes (colors, see Figs. 2,3) and the

1414 actual fraction of synapses made onto these target classes, sampled in cubes of ~5

1415 µm edge length (dots) distributed across the dataset volume (average over entire

1416 dataset, large circles). **(b)** Sketch of the axon-based measurement of the fraction of

1417 surface area of the various subcellular target classes (colors) within a distance r_{pred}

1418 from a given axon (black). **(c)** Example surfaces around two axons (Ax1, Ax2, same

1419 as in Fig. 3g) with r_{pred} = 5 µm (shaded colors: target classes as in a). Ax_1 showed

1420 soma, Ax_2 AD specificity in the analyses in Fig. 3. **(d)** Corresponding surface fraction

1421 of somata and apical dendrites for the two axons in c, in dependence of r_{pred}. **(e)**

1422 Same as (d) for all n=6,979 axons in the dataset, shown separately for the target

1423 classes (see symbols). Colors denote the fraction of synapses of a given axon that

1424 innervate the respective target class. **(f)** Relation between the surface fraction

1425 around all axons and the synaptic innervation by these axons for each target class,

1426 shown for r_{pred} of 10 µm. Black lines show linear regression to obtain optimal model

1427 parameters for geometrical innervation prediction in g. **(g)** Coefficient of

1428 determination (R^2) reporting the fraction of synaptic innervation variance (over all

1429 axons, see f) explained by an innervation model using the available postsynaptic

1430 surface area around axons (shaded area; red, excitatory axons; blue, inhibitory

1431 axons; lower end of shades indicates prediction; upper ends indicate correction by

1432 the variance contributed by the multinomial sampling of targets along axons, see

1433 Methods). Insets (right) show sampling-corrected predictive power of excitatory (top)

1434 and inhibitory (bottom) axons for the innervation of target classes. This analysis

1435 refutes a random geometry-based innervation rule for axons in dense cortical

1436 neuropil.

1437
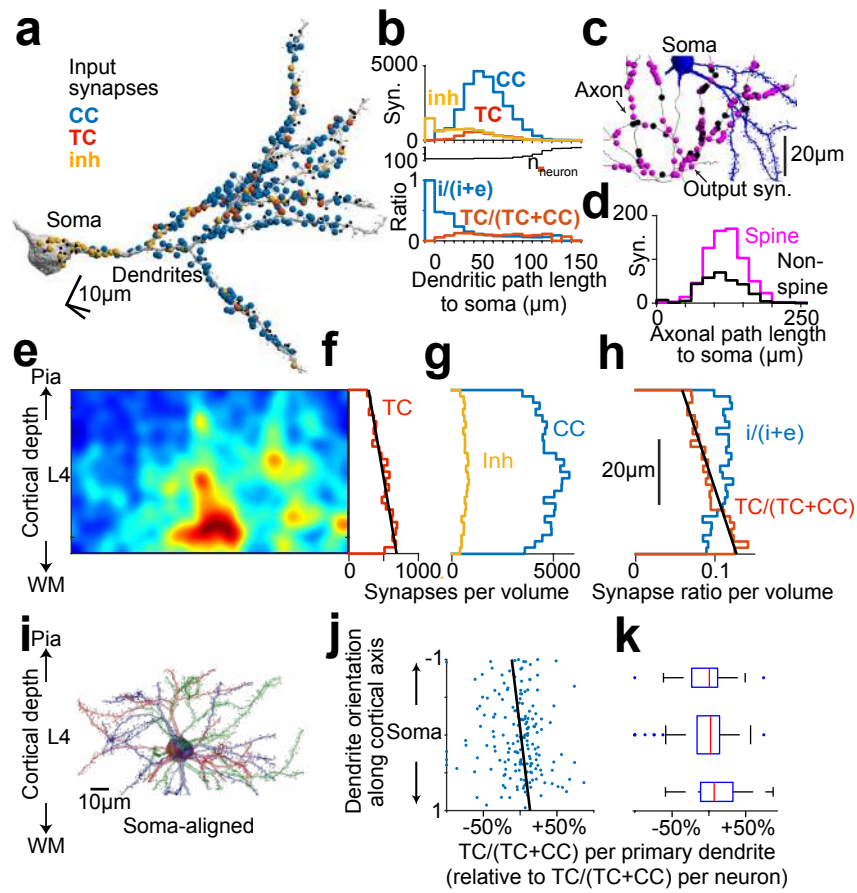
2018 L4 dense
Figure 5

1438 **Figure 5**

1439 **Distribution of synapses along dendrites and axons, and variability of synaptic**

1440 **input composition. (a)** Neuron with cell body and primary dendrites; all input

1441 synapses are indicated, colored according to the type of presynaptic axon (yellow:

1442 inhibitory; red: TC, blue: CC; black, axon with less than 10 synapses). **(b)**

1443 Distribution of input synapses (top) and resulting inhibitory/excitatory balance and TC

1444 input fraction (bottom) summed over all neurons in the dataset (n=90 neurons,

1445 n=183 primary dendrites, total of n=47,552 synapses) as function of dendritic path

1446 length to soma. Black line indicates number of neurons (n_{neuron}) contributing to the

1447 respective distance bin. **(c)** Neuron with soma and local axon collaterals, all output

1448 synapses are indicated according to the target (magenta: spine; black: non-spine).

1449 **(d)** Average distribution of spine and non-spine targets along path length of L4

1450 output axons refuting path-length dependent axonal synapse sorting (PLASS) for L4

1451 of mouse S1 (compare (Schmidt et al., 2017) for mammalian cortex). **(e-h)**

1452 Distribution of TC synapses within L4 dataset (e) shows gradient along the cortical

1453 axis (f), which is absent for inhibitory or CC synapses (g). **(h)** Resulting gradient in

1454 TC synapse fraction (increase by 83% from 7.0% to 12.8% (+5.8%) within 50 µm

1455 along the cortical axis; line fit, $p<1.1x10^{-12}$, n=134,537 synapses). **(i-k)** Analysis of

1456 the variability of TC input onto the primary dendrites of neurons possibly resulting

1457 from the TC synapse gradient (h): example reconstructions (i) aligned to the somata;

1458 (j) fraction of excitatory input synapses originating from TC axons evaluated for each

1459 primary dendrite, plotted according to the direction of the dendrite in relation to the

1460 cortical axis (-1: dendrite aligned towards the pia; +1: dendrite aligned towards the

1461 white matter). The TC input fraction (TC/(TC+CC)) of each dendrite was compared to

1462 the TC input fraction of its entire parent neuron, ratios are shown. (k) Summary

1463 analysis of relation between dendrite direction and relative TC input fraction. Note

1464 that at the level of single dendrites, TC input fraction is determined by the dendrites'

1465 orientation relative to the cortex axis (k, 1.28-fold higher relative TC fraction for

1466 downwards pointing dendrites (projection >0.5) than upwards pointing dendrites

1467 (projection <-0.5), n=183, p=0.026, two-sided t-test for dendrites with a normalized

1468 absolute projection >0.5; bars correspond to dendrites from projection ranges -1..-

1469 0.5; -0.5..0.5; 0.5..1, respectively). This data indicates a synaptic input mixing that

1470 enhances synaptic input variability at the level of single dendrites.

52
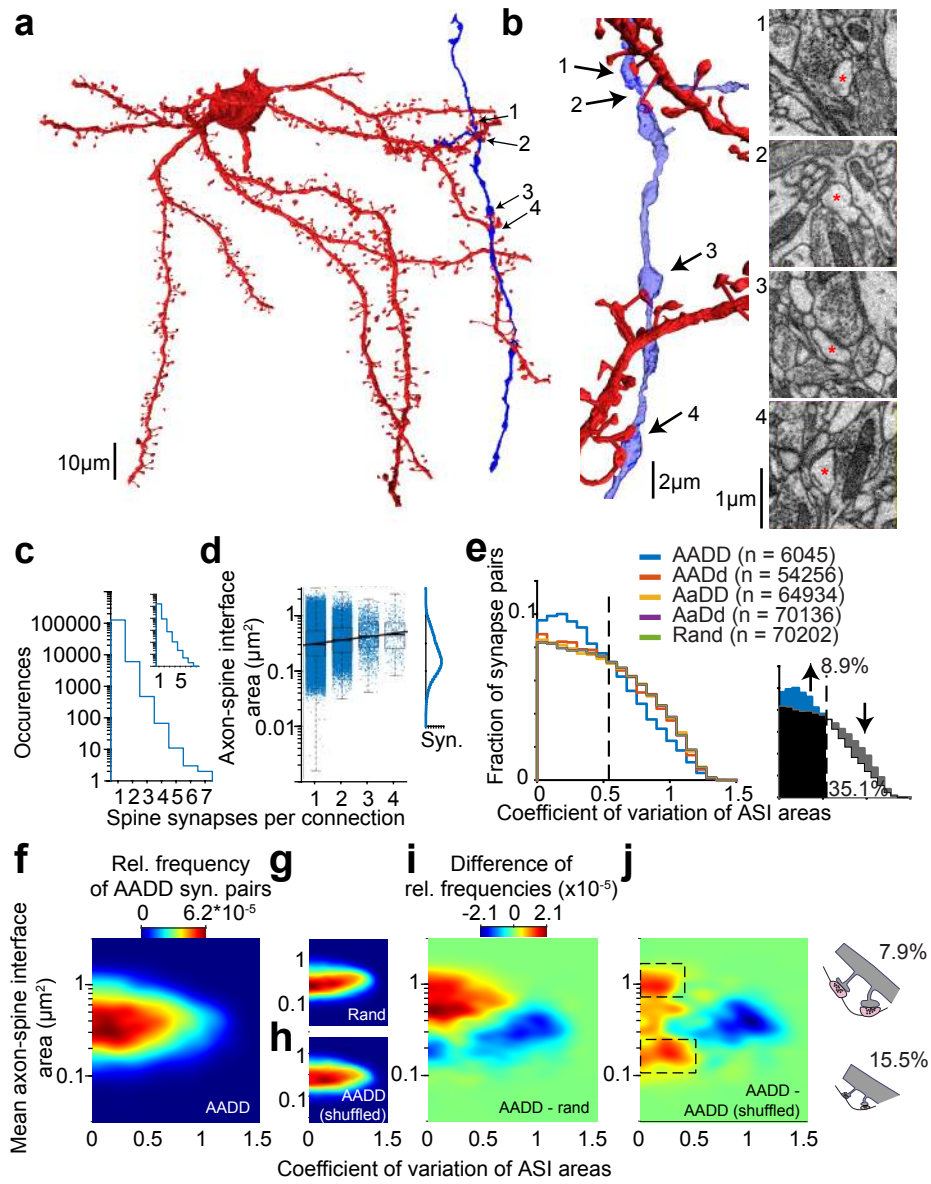
2018 L4 dense
Figure 6

1471 **Figure 6**

1472 **Analysis of multisynaptic connections for spine synapse size homogenization**

1473 **possibly induced by Hebbian learning. (a,b)** Example of an axon innervating the

1474 dendrites of a postsynaptic neuron 4 times within the dataset (b; red asterisks

1475 indicate innervated spine heads). **(c)** Frequency of multi-hit connections. Note that

1476 n=6,045 connections involved 2 synapses, and n=557 at least 3; numbers are for

1477 control reconstruction set, in which all axons were split at branch points to avoid

1478 contamination by axon mergers (unsplit axons in inset); see Methods. **(d)** Distribution

1479 of axon-spine interface (ASI, (de Vivo et al., 2017; Staffler et al., 2017)) size over

1480 single and multi-hit connections indicating larger synapses in multisynaptically

1481 connected pairs. Inset: overall single synapse ASI size distribution following a log-

1482 normal distribution. **(e)** Analysis of synapse size similarity for pairs of synapses

1483 drawn randomly (rand, green) and from unrelated axons and dendrites (AaDd,

1484 purple), pairs of same axon but different dendrites (AADd, red), same dendrite but

1485 different axons (AaDD, yellow), and same axon – same dendrites (AADD, blue). The

1486 distribution of synaptic size variability (coefficient of variation) for pairs of randomly

1487 drawn synapses and for those involved in AADD connections shows that low-

1488 variance connections are over-represented (inset). Based on the fraction of axons

1489 with less-than expected variability, one can obtain the intersection point on the CV

1490 axis (dashed line, CV=0.54) and estimate the fraction of axon-dendrite pairs in the

1491 circuit that could have undergone Hebbian learning as at least 8.9%, whereas at

1492 least 35.1% show no sign of CV reduction possibly induced by Hebbian learning-

1493 related plasticity (inset). **(f-j)** Analysis of relation between highly consistent

1494 connections and average synapse size (f) in comparison to randomly drawn pairs of

1495 synapses from the entire synapse population (g) and in comparison to synapse pairs

1496 drawn randomly from the joint synapse population (h). Difference maps (i,j) show

1497 that in fact low-CV synapse pairs and larger synapse size are correlated (i); and that

1498 two populations of overrepresented low-CV synapses can be described (j, dashed

1499 areas); possibly corresponding to synapses with a history of LTP (up to 7.9%) and a

1500 small connection type or history of LTD (up to 15.5%).

1501

53

REFERENCES

Ahmed, B., Anderson, J.C., Douglas, R.J., Martin, K.A., and Nelson, J.C. (1994). Polyneuronal innervation of spiny stellate neurons in cat visual cortex. The Journal of comparative neurology *341*, 39-49.

Bartol, T.M., Bromer, C., Kinney, J., Chirillo, M.A., Bourne, J.N., Harris, K.M., and Sejnowski, T.J. (2015). Nanoconnectomic upper bound on the variability of synaptic plasticity. Elife *4*, e10778.

Benshalom, G., and White, E.L. (1986). Quantification of thalamocortical synapses with spiny stellate neurons in layer IV of mouse somatosensory cortex. The Journal of comparative neurology *253*, 303-314.

Berning, M., Boergens, K.M., and Helmstaedter, M. (2015). SegEM: Efficient Image Analysis for High-Resolution Connectomics. Neuron *87*, 1193-1206.

Binzegger, T., Douglas, R.J., and Martin, K.A. (2004). A quantitative map of the circuit of cat primary visual cortex. J Neurosci *24*, 8441-8453.

Bloss, E.B., Cembrowski, M.S., Karsh, B., Colonell, J., Fetter, R.D., and Spruston, N. (2018). Single excitatory axons form clustered synapses onto CA1 pyramidal cell dendrites. Nat Neurosci *21*, 353-363.

Boergens, K.M., Berning, M., Bocklisch, T., Braunlein, D., Drawitsch, F., Frohnhofen, J., Herold, T., Otto, P., Rzepka, N., Werkmeister, T.*, et al.* (2017). webKnossos: efficient online 3D data annotation for connectomics. Nat Methods *14*, 691-694.

Bopp, R., Holler-Rickauer, S., Martin, K.A., and Schuhknecht, G.F. (2017). An Ultrastructural Study of the Thalamic Input to Layer 4 of Primary Motor and Primary Somatosensory Cortex in the Mouse. J Neurosci *37*, 2435-2448.

Braitenberg, V., and Schüz, A. (1998). Cortex: Statistics and Geometry of Neuronal Connectivity (Berlin Heidelberg: Springer).

1529 Brecht, M., and Sakmann, B. (2002). Dynamic representation of whisker deflection
1530 by synaptic potentials in spiny stellate and pyramidal cells in the barrels and septa of
1531 layer 4 rat somatosensory cortex. J Physiol *543*, 49-70.

1532 Briggman, K.L., Helmstaedter, M., and Denk, W. (2011). Wiring specificity in the
1533 direction-selectivity circuit of the retina. Nature *471*, 183-188.

1534 Bromer, C., Bartol, T.M., Bowden, J.B., Hubbard, D.D., Hanka, D.C., Gonzalez, P.V.,
1535 Kuwajima, M., Mendenhall, J.M., Parker, P.H., Abraham, W.C.*, et al.* (2018). Long-
1536 term potentiation expands information content of hippocampal dentate gyrus
1537 synapses. Proc Natl Acad Sci U S A *115*, E2410-E2418.

1538 Cardona, A., Saalfeld, S., Schindelin, J., Arganda-Carreras, I., Preibisch, S., Longair,
1539 M., Tomancak, P., Hartenstein, V., and Douglas, R.J. (2012). TrakEM2 software for
1540 neural circuit reconstruction. PLoS One *7*, e38011.

1541 Carr, C.E., and Konishi, M. (1988). Axonal delay lines for time measurement in the
1542 owl's brainstem. Proc Natl Acad Sci U S A *85*, 8311-8315.

1543 Carr, C.E., and Konishi, M. (1990). A circuit for detection of interaural time
1544 differences in the brain stem of the barn owl. J Neurosci *10*, 3227-3246.

1545 Corney, J., Rea, H., Clark, D., Pritchard, J., Breaks, M., and Macleod, R. (2002).
1546 Coarse filters for shape matching. IEEE Computer Graphics and Applications *22*, 65-
1547 74.

1548 da Costa, N.M., and Martin, K.A. (2009). The proportion of synapses formed by the
1549 axons of the lateral geniculate nucleus in layer 4 of area 17 of the cat. The Journal of
1550 comparative neurology *516*, 264-276.

1551 de Vivo, L., Bellesi, M., Marshall, W., Bushong, E.A., Ellisman, M.H., Tononi, G., and
1552 Cirelli, C. (2017). Ultrastructural evidence for synaptic scaling across the wake/sleep
1553 cycle. Science *355*, 507-510.

1554 Denk, W., and Horstmann, H. (2004). Serial block-face scanning electron
1555 microscopy to reconstruct three-dimensional tissue nanostructure. PLoS biology *2*,
1556 e329.

Dorkenwald, S., Schubert, P.J., Killinger, M.F., Urban, G., Mikula, S., Svara, F., and Kornfeld, J. (2017). Automated synaptic connectivity inference for volume electron microscopy. Nat Methods *14*, 435-442.

Egger, V., Feldmeyer, D., and Sakmann, B. (1999). Coincidence detection and changes of synaptic efficacy in spiny stellate neurons in rat barrel cortex. Nature neuroscience *2*, 1098-1105.

Eichler, K., Li, F., Litwin-Kumar, A., Park, Y., Andrade, I., Schneider-Mizell, C.M., Saumweber, T., Huser, A., Eschbach, C., Gerber, B*., et al.* (2017). The complete connectome of a learning and memory centre in an insect brain. Nature *548*, 175-182.

Feldmeyer, D., Egger, V., Lubke, J., and Sakmann, B. (1999). Reliable synaptic connections between pairs of excitatory layer 4 neurones within a single 'barrel' of developing rat somatosensory cortex. J Physiol *521 Pt 1*, 169-190.

Feldmeyer, D., Lubke, J., Silver, R.A., and Sakmann, B. (2002). Synaptic connections between layer 4 spiny neurone-layer 2/3 pyramidal cell pairs in juvenile rat barrel cortex: physiology and anatomy of interlaminar signalling within a cortical column. J Physiol *538*, 803-822.

Friedman, J., Hastie, T., and Tibshirani, R. (2000). Additive logistic regression: a statistical view of boosting (With discussion and a rejoinder by the authors). Ann Statist *28*, 337-407.

Garcia-Marin, V., Ahmed, T.H., Afzal, Y.C., and Hawken, M.J. (2013). Distribution of vesicular glutamate transporter 2 (VGluT2) in the primary visual cortex of the macaque and human. The Journal of comparative neurology *521*, 130-151.

Garcia-Marin, V., Kelly, J.G., and Hawken, M.J. (2017). Major Feedforward Thalamic Input Into Layer 4C of Primary Visual Cortex in Primate. Cereb Cortex, 1-16.

Han, Y., Kebschull, J.M., Campbell, R.A.A., Cowan, D., Imhof, F., Zador, A.M., and Mrsic-Flogel, T.D. (2018). The logic of single-cell projections from visual cortex. Nature *556*, 51-56.

56

Harris, K.M., and Stevens, J.K. (1988). Dendritic spines of rat cerebellar Purkinje cells: serial electron microscopy with reference to their biophysical characteristics. J Neurosci *8*, 4455-4469.

Harris, K.M., and Stevens, J.K. (1989). Dendritic spines of CA 1 pyramidal cells in the rat hippocampus: serial electron microscopy with reference to their biophysical characteristics. J Neurosci *9*, 2982-2997.

Hebb, D.O. (1949). The Organization of Behavior (New York: Wiley).

Helmstaedter, M., Briggman, K.L., and Denk, W. (2011). High-accuracy neurite reconstruction for high-throughput neuroanatomy. Nat Neurosci *14*, 1081-1088.

Helmstaedter, M., Briggman, K.L., Turaga, S.C., Jain, V., Seung, H.S., and Denk, W. (2013). Connectomic reconstruction of the inner plexiform layer in the mouse retina. Nature *500*, 168-174.

Hua, Y., Laserstein, P., and Helmstaedter, M. (2015). Large-volume en-bloc staining for electron microscopy-based connectomics. Nat Commun *6*, 7923.

Januszewski, M., Kornfeld, J., Li, P.H., Pope, A., Blakely, T., Lindsey, L., Maitin-Shepard, J., Tyka, M., Denk, W., and Jain, V. (2018). High-precision automated reconstruction of neurons with flood-filling networks. Nat Methods *15*, 605-610.

Jeffress, L.A. (1948). A place theory of sound localization. Journal of comparative and physiological psychology *41*, 35-39.

Kasthuri, N., Hayworth, K.J., Berger, D.R., Schalek, R.L., Conchello, J.A., Knowles-Barley, S., Lee, D., Vazquez-Reina, A., Kaynig, V., Jones, T.R.*, et al.* (2015). Saturated Reconstruction of a Volume of Neocortex. Cell *162*, 648-661.

Kerr, J.N., de Kock, C.P., Greenberg, D.S., Bruno, R.M., Sakmann, B., and Helmchen, F. (2007). Spatial organization of neuronal population responses in layer 2/3 of rat barrel cortex. J Neurosci *27*, 13316-13328.

Kerr, J.N., Greenberg, D., and Helmchen, F. (2005). Imaging input and output of neocortical networks in vivo. Proc Natl Acad Sci U S A *102*, 14063-14068.

1612 Ko, H., Hofer, S.B., Pichler, B., Buchanan, K.A., Sjostrom, P.J., and Mrsic-Flogel,
1613 T.D. (2011). Functional specificity of local synaptic connections in neocortical
1614 networks. Nature *473*, 87-91.

1615 Kornfeld, J., Benezra, S.E., Narayanan, R.T., Svara, F., Egger, R., Oberlaender, M.,
1616 Denk, W., and Long, M.A. (2017). EM connectomics reveals axonal target variation
1617 in a sequence-generating network. Elife *6*, e24364

1618 Kubota, Y., Karube, F., Nomura, M., and Kawaguchi, Y. (2016). The Diversity of
1619 Cortical Inhibitory Synapses. Front Neural Circuits *10*, 27.

1620 Latawiec, D., Martin, K.A., and Meskenaite, V. (2000). Termination of the
1621 geniculocortical projection in the striate cortex of macaque monkey: a quantitative
1622 immunoelectron microscopic study. The Journal of comparative neurology *419*, 306-
1623 319.

1624 Lavzin, M., Rapoport, S., Polsky, A., Garion, L., and Schiller, J. (2012). Nonlinear
1625 dendritic processing determines angular tuning of barrel cortex neurons in vivo.
1626 Nature *490*, 397-401.

1627 Lee, W.C., Bonin, V., Reed, M., Graham, B.J., Hood, G., Glattfelder, K., and Reid,
1628 R.C. (2016). Anatomy and function of an excitatory network in the visual cortex.
1629 Nature *532*, 370-374.

1630 Lubke, J., Egger, V., Sakmann, B., and Feldmeyer, D. (2000). Columnar
1631 organization of dendrites and axons of single and synaptically coupled excitatory
1632 spiny neurons in layer 4 of the rat barrel cortex. J Neurosci *20*, 5300-5311.

1633 Lubke, J., Roth, A., Feldmeyer, D., and Sakmann, B. (2003). Morphometric analysis
1634 of the columnar innervation domain of neurons connecting layer 4 and layer 2/3 of
1635 juvenile rat barrel cortex. Cereb Cortex *13*, 1051-1063.

1636 Markram, H., Lubke, J., Frotscher, M., and Sakmann, B. (1997). Regulation of
1637 synaptic efficacy by coincidence of postsynaptic APs and EPSPs. Science *275*, 213-
1638 215.

1639 Markram, H., Muller, E., Ramaswamy, S., Reimann, M.W., Abdellah, M., Sanchez,
1640 C.A., Ailamaki, A., Alonso-Nanclares, L., Antille, N., Arsever, S*., et al.* (2015).
1641 Reconstruction and Simulation of Neocortical Microcircuitry. Cell *163*, 456-492.

1642 McGuire, B.A., Hornung, J.P., Gilbert, C.D., and Wiesel, T.N. (1984). Patterns of
1643 synaptic input to layer 4 of cat striate cortex. J Neurosci *4*, 3021-3033.

1644 Meyer, H.S., Wimmer, V.C., Hemberger, M., Bruno, R.M., de Kock, C.P., Frick, A.,
1645 Sakmann, B., and Helmstaedter, M. (2010). Cell type-specific thalamic innervation in
1646 a column of rat vibrissal cortex. Cereb Cortex *20*, 2287-2303.

1647 Mishchenko, Y., Hu, T., Spacek, J., Mendenhall, J., Harris, K.M., and Chklovskii,
1648 D.B. (2010). Ultrastructural analysis of hippocampal neuropil from the connectomics
1649 perspective. Neuron *67*, 1009-1020.

1650 Oberlaender, M., Boudewijns, Z.S., Kleele, T., Mansvelder, H.D., Sakmann, B., and
1651 de Kock, C.P. (2011). Three-dimensional axon morphologies of individual layer 5
1652 neurons indicate cell type-specific intracortical pathways for whisker motion and
1653 touch. Proc Natl Acad Sci U S A *108*, 4188-4193.

1654 Oberlaender, M., de Kock, C.P., Bruno, R.M., Ramirez, A., Meyer, H.S., Dercksen,
1655 V.J., Helmstaedter, M., and Sakmann, B. (2012a). Cell type-specific three-
1656 dimensional structure of thalamocortical circuits in a column of rat vibrissal cortex.
1657 Cereb Cortex *22*, 2375-2391.

1658 Oberlaender, M., Ramirez, A., and Bruno, R.M. (2012b). Sensory experience
1659 restructures thalamocortical axons during adulthood. Neuron *74*, 648-655.

1660 Ohki, K., Chung, S., Ch'ng, Y.H., Kara, P., and Reid, R.C. (2005). Functional imaging
1661 with cellular resolution reveals precise micro-architecture in visual cortex. Nature
1662 *433*, 597-603.

1663 Osada, R., Funkhouser, T., Chazelle, B., and Dobkin, D. (2001). Matching 3D
1664 models with shape distributions. Paper presented at: Proceedings International
1665 Conference on Shape Modeling and Applications.

Preibisch, S., Saalfeld, S., and Tomancak, P. (2009). Globally optimal stitching of tiled 3D microscopic image acquisitions. Bioinformatics *25*, 1463-1465.

Rolnick, D., and Shavit, N. (2017). Morphological Error Detection in 3D Segmentations. arXiv *1705.10882v1*.

Schmidt, H., Gour, A., Straehle, J., Boergens, K.M., Brecht, M., and Helmstaedter, M. (2017). Axonal synapse sorting in medial entorhinal cortex. Nature *549*, 469-475.

Schneider-Mizell, C.M., Gerhard, S., Longair, M., Kazimiers, T., Li, F., Zwart, M.F., Champion, A., Midgley, F.M., Fetter, R.D., Saalfeld, S*., et al.* (2016). Quantitative neuroanatomy for connectomics in Drosophila. Elife *5*.

Shepherd, G.M., and Harris, K.M. (1998). Three-dimensional structure and composition of CA3-->CA1 axons in rat hippocampal slices: implications for presynaptic connectivity and compartmentalization. J Neurosci *18*, 8300-8310.

Staffler, B., Berning, M., Boergens, K.M., Gour, A., van der Smagt, P., and Helmstaedter, M. (2017). SynEM, automated synapse detection for connectomics. Elife *6*, e26414.

Storey, J.D., and Tibshirani, R. (2003). Statistical significance for genomewide studies. Proc Natl Acad Sci U S A *100*, 9440-9445.

Stosiek, C., Garaschuk, O., Holthoff, K., and Konnerth, A. (2003). In vivo two-photon calcium imaging of neuronal networks. Proc Natl Acad Sci U S A *100*, 7319-7324.

Taniguchi, H., Lu, J., and Huang, Z.J. (2013). The spatial and temporal origin of chandelier cells in mouse neocortex. Science *339*, 70-74.

Wanner, A.A., Genoud, C., and Friedrich, R.W. (2016a). 3-dimensional electron microscopic imaging of the zebrafish olfactory bulb and dense reconstruction of neurons. Sci Data *3*, 160100.

Wanner, A.A., Genoud, C., Masudi, T., Siksou, L., and Friedrich, R.W. (2016b). Dense EM-based reconstruction of the interglomerular projectome in the zebrafish olfactory bulb. Nat Neurosci *19*, 816-825.

1693   White, E.L. (1989). Cortical Circuits: Synaptic Organization of the Cerebral Cortex;
1694   Structure, Function and Theory (Boston: Birkhauser).

1695   White, E.L., and Hersch, S.M. (1981). Thalamocortical synapses of pyramidal cells
1696   which project from SmI to MsI cortex in the mouse. The Journal of comparative
1697   neurology *198*, 167-181.

1698   Wimmer, V.C., Bruno, R.M., de Kock, C.P., Kuner, T., and Sakmann, B. (2010).
1699   Dimensions of a projection column and architecture of VPM and POm axons in rat
1700   vibrissal cortex. Cereb Cortex *20*, 2265-2276.

1701   Yi, L., Jiantao, P., Hongbin, Z., Liu, W., and Uehara, Y. (2004). Thickness histogram
1702   and statistical harmonic representation for 3D model retrieval. Paper presented at:
1703   Proceedings 2nd International Symposium on 3D Data Processing, Visualization and
1704   Transmission, 2004 3DPVT 2004.

1705   Zung, J., Tartavull, I., Lee, K., and Seung, H.S. (2017). An Error Detection and
1706   Correction Framework for Connectomics. NIPS *2017*.

1707